Computational modelling of gas liquid solid multiphase free surface flow with and without evaporation

Huihuang Xia*, Marc Kamlah

Institute for Applied Materials (IAM), Karlsruhe Institute of Technology (KIT), Hermann-von Helmholtz-Platz 1 76344 Eggenstein-Leopoldshafen, Germany

ARTICLE INFO

Article history:
Received 17 August 2023
Received in revised form
17 November 2023
Accepted 8 December 2023
Available online 19 December 2023

Keywords:
Capillary force
Discrete element method
Liquid bridge
Particle transport
Resolved CFD-DEM
Volume of fluid

ABSTRACT

Gas liquid solid multiphase systems are ubiquitous in engineering applications, e.g. inkjet printing, spray drying and coating. Developing a numerical framework for modelling these multiphase systems is of great significance. An improved, resolved computational fluid dynamics discrete element method (CFD DEM) framework is developed to model the multiphase free surface flow with and without evaporation. An improved capillary force model is developed to compute the capillary interactions for partially floating particles at a free surface. Three well known benchmark cases, namely drag coefficient calculation, the single sphere settling, and drafting kissing tumbling of two particles are conducted to validate the resolved CFD DEM model. It turns out that the resolved CFD DEM model developed in this paper can accurately calculate the fluid solid interactions and predict the trajectory of solid particles interacting with the liquid phase. Numerical demonstrations, namely two particles moving along a free surface when the liquid phase evaporates, and particle transport and accumulations inside an evaporating sessile droplet show the performance of the resolved model.

1. Introduction

Granular materials widely exist in our daily life (e.g. sugar, salt and coffee bins) and industry (e.g. coal, sand and bearing balls). However, some granular materials are surrounded by fluids such as gases or liquids (e.g. pneumatic conveying (Kuang, Zhou, & Yu, 2020), fluidized beds (Zhang et al., 2023), mudflow (Fang, Wang, Hong, & Zhao, 2022), capillary suspensions (Koos, 2014) and more (Golshan et al., 2020; Lu, Gao, Dietiker, Shahnam, & Rogers, 2022; Ma et al., 2022)). Computational modelling of these kinds of gas–liquid–solid multiphase systems is of great importance for better understanding the complex interactions among solid particles and between the solid phase (particles) and the fluid phase (liquids or gases).

The discrete element method (DEM) is capable of modelling the complex mechanical behaviour of solid particles and the interactions between a particle and a wall. The motion of solid particles in different scales, namely macro , meso and micro scale, can be tracked by solving Newton's second law of motion. Computational fluid dynamics (CFD) is generally used to model the motion of fluids by solving the Navier Stokes equations. The so called coupling approach, namely coupling CFD to DEM (CFD DEM), is widely used to model the complex interaction between solid and fluid phases, as discussed below.

In this work, the resolved CFD DEM approach is discussed. In the resolved CFD DEM approach, the motions of solid and fluid phases are governed by DEM and CFD, respectively (Balachandran Nair, Pirker, & Saeedipour, 2021). Modelling enables us to understand multiphase systems at different scales, and extensive parameter studies can be conducted to investigate the influence of operating parameters at a lower cost. During the past decades, the CFD DEM approach has been widely used to computationally model either compressible or incompressible particle laden flow (Hager, Kloss, Pirker, & Goniva, 2014; Podlozhnyuk, 2018; Zhao, 2014). Hager et al. developed a simple method for smooth representation of the void fraction field for multi scale resolved CFD DEM simulations (Hager, 2014; Hager et al., 2014). Podlozhnyuk implemented the superquadric particles into the resolved CFD DEM (Podlozhnyuk, 2018). Davydzenka et al. developed a resolved CFD DEM model accounting for the wettability of complex geometry in multiphase flow (Davydzenka, Fagbemi, & Tahmasebi, 2020). Blood flow with irregular red blood cell particles was investigated within the resolved CFD DEM framework by

* Corresponding author.
E-mail address: huihuang.xia@kit.edu (H. Xia).

Nomenclature

Constants

$\mathbf{g}$	Gravitational acceleration constant [m/s^2]

Greek letters

Γ	Boundary
θ	Contact angle
ρ	Density [kg/m^3]
μ	Dynamic viscosity [Pa s]
Σ	Total stress tensor
τ	Viscous stress tensor
α	Volume fraction [ ]

Other symbols

$\mathbf{F}$	Force
$\mathbf{I}$	Identity tensor
$\dot{m}$	Mass source per unit volume [kg/(m^3 ·s)]
m	Mass
$\mathbf{n}$	Normal vector
$\mathbf{x}_i$	Position vector
p	Pressure [Pa]
ϵ_s	Solid fraction [ ]
$\mathbf{t}$	Tangent vector
$\mathbf{M}$	Torque
$\mathbf{t}_{\Gamma_s}$	Traction vector
D_v	Vapour diffusion coefficient [m^2/s]
Y	Vapour mass fraction [ ]
$\mathbf{U}$	Velocity [m/s]
ϵ_f	Void fraction [ ]

Subscripts

cp	Capillary
evap	Evaporation
fp	Fluid particle
g	Gas
l	Liquid
ij	Particle i particle j
pf	Particle fluid
s	Solid
st	Surface tension
i	The ith particle

Balachandran et al. (Balachandran Nair et al., 2021). Free surface flow with capillary interactions was studied by Nguyen et al., where a capillary force model was developed (Nguyen, Chan, Tsuji, Tanaka, & Washino, 2021). Flow with irregular particles constructed with multi sphere clumps in an incompressible free surface flow was investigated by Shen et al. (Shen, Wang, Huang, & Jin, 2022). Melting of solid particles for selective laser melting was computa tionally modelled by an improved resolved CFD DEM approach developed by Yu et al. (Yu & Zhao, 2021). Schnorr Filho et al. investigated the hydraulic conveying of solid particles through a narrow elbow with a resolved CFD DEM model (Schnorr Filho, Lima, & Franklin, 2022). Free surface flow with superquadric par ticles was investigated by Washino et al., with the capillary force incorporated into the resolved CFD DEM model (Washino, Chan, Tsujimoto, Tsuji, & Tanaka, 2023).

A summary of numerical simulations and applications of existing resolved CFD DEM approaches is listed in Table 1. How ever, what can be seen from the table is that a limited number of publications can be found related to model solid particles immersed in an incompressible flow that undergoes phase change or evaporation. Direct inkjet printing (Derby, 2015; Lohse, 2022), spray drying (Giuliano, Buffo, Vanni, & Frungieri, 2023; Yang et al., 2023) and spray coating (Christodoulou, Sorensen, Khair, García Munoz, & Mazzei, 2020; Kieckhefen, Lichtenegger, Pietsch, Pirker, & Heinrich, 2019) involve complex solid liquid interactions, the phase change from liquid to vapour, surface tension and beyond. Accordingly, developing such a numerical model accounting for additional phase change and surface ten sion is of great significance.

In this paper, an improved resolved CFD DEM framework incorporating free surface capturing, surface tension and phase change of the liquid phase is developed by extending the resolved CFD DEM model developed by Hager et al. (Hager, 2014; Hager et al., 2014). The new resolved CFD DEM framework is imple mented in the open source framework CFDEMcoupling PUBLIC (D. Computing and CFDEM®coupling, 2017) bridging the open source DEM code LIGGGHTS (D. Computing and LIGGGHTS, 2015) and the open source finite volume method based C++ library Open FOAM (O. Foundation, 2018). The large scale parallel computation and data exchange between the two codes are realized using the message passing interface software (Gabriel et al., 2004).

This paper consists of the following sections: the mathematical formulation, namely the governing equations for the liquid and solid phases, are presented in Section 2. The detailed numerical method for solving these governing equations, numerical proced ure and coupling algorithm are discussed in Section 3. In Section 4, the numerical validations and demonstrations are presented. The conclusions of this paper are summarized in Section 5. Some additional contents are discussed in the Appendix of this paper for completeness.

Table 1
Summary and comparison among these applications of resolved CFD-DEM formulations.

Authors (publication year)	Applications	Surface tension	Phase change
Hager et al. (2014) (Hager, 2014)	Multi-scale modelling	no	no
Podlozhnyuk, Pirker, and Kloss (2017)	Flow with superquadric particles	no	no
Davydzenka et al. (2020)	Multiphase flow in porous media	yes	no
Balachandran Nair et al. (2021)	Blood flow in microfluidic devices	no	no
Nguyen et al. (2021)	Flow with capillary interactions	yes	no
Shen et al. (2022)	Flow with irregular particles	yes	no
Yu & Zhao (2021)	Selective laser melting	yes	yes
Schnorr Filho et al. (2022)	Hydraulic conveying	no	no
Washino et al. (2023)	Flow with non-spherical particles	yes	no

2. Mathematical formulation

In this section, the theory and mathematical formulation of the resolved CFD DEM approach are introduced in detail. For the resolved CFD DEM approach, one solid particle usually occupies several CFD cells (see the inset on the top left of Fig. 1). Here, the CFD cell refers to a small computational cell bounded by arbitrary polygonal faces after discretizing the computational domain, numerically. The void fraction field ϵ_f is used to quantify how much volume is not occupied by a solid particle in each CFD cell because of which ϵ_f 0 indicates that a solid particle fully covers the current CFD cell. The free surface is captured by the improved algebraic VoF method incorporated in the i CLSVoF framework presented in our previous work (Xia & Kamlah, 2024; Xia, 2023). The i CLSVoF framework captures a sharp interface with less interface diffusion. Also, an improved surface tension force model has been developed and implemented in our i CLSVoF model. The Fictitious Domain Method developed by Patankar et al. (Patankar, Singh, Joseph, Glowinski, & Pan, 2000) was extended to incor porate the free surface capturing, surface tension and evaporation for modelling the complex multiphase system as demonstrated by Fig. 1.

As shown in Fig. 2, Ω is the whole computational domain, and Ω_f and Ω_s are the liquid and solid phases, respectively. Γ and Γ_s denote the boundaries of the whole computational domain and the solid particles immersed in the liquid, respectively. The governing equations for the surface tension dominant incompressible New tonian flow are given by

$$\nabla\cdot\mathbf{U} \quad \epsilon_f\dot{m}\left(\frac{1}{\rho_g} \quad \frac{1}{\rho_l}\right) \text{ in } \Omega, \tag{1}$$

$$\frac{\partial(\rho\mathbf{U})}{\partial t}+\nabla\cdot(\rho\mathbf{U}\mathbf{U}) \qquad \nabla p+\nabla\cdot\left[\mu\left(\nabla\mathbf{U}+(\nabla\mathbf{U})^{\mathrm{T}}\right)\right]+\rho\mathbf{g} +\mathbf{F}_{\mathrm{st}} \text{ in } \Omega, \tag{2}$$

where ϵ_f is the void fraction field. The incorporation of ϵ_f is to guarantee that phase change or evaporation of the liquid phase does not occur inside solid particles. $\dot{m}$ in the continuity equa tion (Eq. (1)) is the mass source term per unit volume, where $\dot{m}$ 0 holds for the case without evaporation or phase change only. Furthermore, some other terms, e.g. pressure gradient ∇p and surface tension force $\mathbf{F}_{\mathrm{st}}$ in the momentum equation (Eq. (2)), are detailed in our previous work (Xia & Kamlah, 2024; Xia, 2023).

The governing equations and numerical method for the computational modelling of droplet evaporation are detailed in our previous work (Xia & Kamlah, 2024; Xia, 2023). In our previous work, detailed information regarding equations, methods, numerical implementations and validations for modelling surface tension dominant droplet evaporation are discussed. This section only mentions some basic equations for modelling evaporation. The vapour mass fraction gradient model discussed in our previous work is used in this paper. The vapour mass fraction Y is solved from

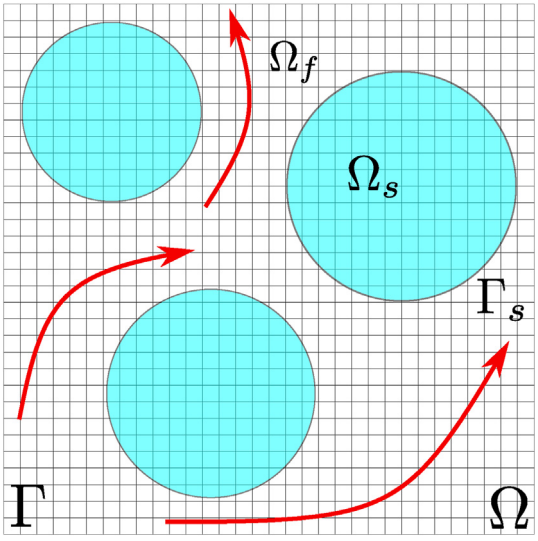

Fig. 2. The schematic diagram of the resolved CFD-DEM model. Arrows represent the vectors of fluid velocity around particles, and circles in blue represent solid particles. CFD-DEM, computational fluid dynamics-discrete element method.

$$\frac{\partial Y}{\partial t}+\nabla\cdot(Y\mathbf{U}) \quad D_v\nabla^2 Y, \tag{3}$$

where D_v is the vapour diffusion coefficient (Xia & Kamlah, 2024; Xia, 2023). The mass source term $\dot{m}$ in the continuity equation (Eq. (1)) is calculated by

$$\dot{m} \quad \frac{\rho_g D_v\nabla^{\Gamma}Y\mathbf{n}^{\Gamma}}{1 \quad Y^{\Gamma}}|\nabla\alpha_l|, \tag{4}$$

where α_l is the liquid volume fraction field. $\mathbf{n}^{\Gamma}$ is the unit interface normal and ∇^{Γ} denotes the gradient at the interface. Additionally, Y^{Γ} is the saturation vapour mass fraction, which is given by the Clausius–Clapeyron relation (Palmore & Desjardins, 2019). Detailed numerical issues of the evaporation model are discussed in our previous work (Xia & Kamlah, 2024; Xia, 2023).

Newton's second law of motion governs the motion of solid particles. The equation for the translational motion is given by

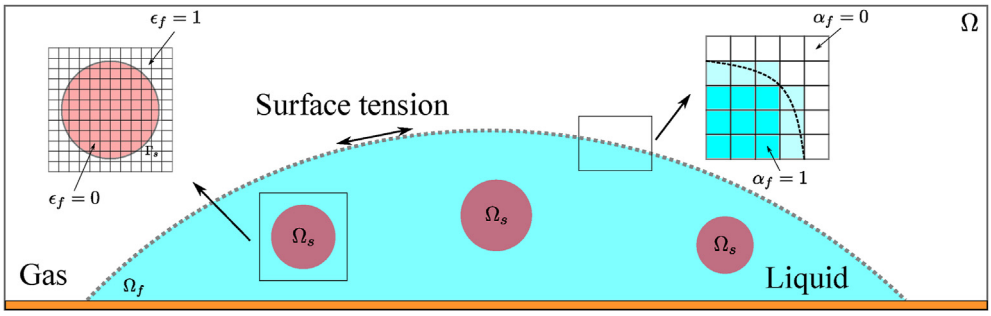

Fig. 1. The schematic diagram of a surface-tension-dominant gas liquid solid multiphase system.

$$m_i \frac{\partial^2 \mathbf{x}_i}{\partial t^2} \quad \sum_{i\ 1}^{N_p} \mathbf{F}_{ij} + m_i \mathbf{g} + \mathbf{F}_{\mathrm{fp}}^{\mathrm{c}} + \mathbf{F}_{\mathrm{cp}}, \tag{5}$$

where m_i and $\mathbf{x}_i$ are the mass and position vector of the ith particle, respectively, $\mathbf{F}_{ij}$ is the contact force between two DEM elements (particle−particle or particle−wall), and $\mathbf{F}_{\mathrm{fp}}^{\mathrm{c}}$ the CFD DEM coupling force acting on the solid particles by the liquid phase. The last term on the right hand side of Eq. (5) is the capillary force acting on solid particles, which is discussed in the next section in detail. Besides, the rotational motion of solid particles is governed by

$$I_i \frac{\partial^2 \boldsymbol{\theta}_i}{\partial t^2} \quad \sum_{i\ 1}^{N_p} \mathbf{M}_{ij} + \mathbf{M}_{\mathrm{fp}}^{\mathrm{c}} + \mathbf{M}_{\mathrm{cp}}, \tag{6}$$

where I_i and $\boldsymbol{\theta}_i$ are the moment of inertia and angular displacement of the particle i, respectively. $\mathbf{M}_{ij}$ is the torque acting on particle i by some other particles interacting with it. $\mathbf{M}_{\mathrm{fp}}^{\mathrm{c}}$ is the coupling term accounting for the torque acting on the solid phase by the liquid phase. The last term $\mathbf{M}_{\mathrm{cp}}$ on the right hand side of Eq. (6) is the torque acting on the particle i due to capillary interactions. Calcu lations of these terms are introduced in the forthcoming sections.

3. Numerical method

Accurate calculations of interaction forces acting on the solid phase by the liquid phase are of great importance for realizing the resolved CFD DEM.

3.1. Calculations of the interaction forces and torque

In the Fictitious Domain Method, additional boundary and interface conditions are needed to be applied due to the presence of solid particles in the liquid phase (Shirgaonkar, MacIver, & Patankar, 2009). These additional conditions are given by

$$\begin{cases} \mathbf{U} \quad \mathbf{U}_\Gamma \text{ on } \Gamma, \\ \mathbf{U} \quad \mathbf{U}_i \text{ on } \Omega_s, \\ \boldsymbol{\Sigma}\cdot\mathbf{n} \quad \mathbf{t}_{\Gamma_s} \text{ on } \Gamma_s, \\ \mathbf{U}(\mathbf{x},\ t \quad 0) \quad \mathbf{U}_0(\mathbf{x}) \text{ in } \Omega_f. \end{cases} \tag{7}$$

Here, the subscript i indicates the ith particle and $\boldsymbol{\Sigma}$ is the total stress tensor as discussed below, and $\mathbf{n}$ is the outward normal vector to Γ_s. $\mathbf{t}_{\Gamma_s}$ is the traction vector acting from the liquid phase on the surface of solid particles. The second and third equations of Eq. (7) are responsible for the coupling between liquid and solid phases. Additionally, the second equation ensures the transfer of the particle velocity $\mathbf{U}_i$ to the liquid velocity of CFD cells covered by the solid particle i. The third equation represents the force acting on the boundaries of the solid phase.

The force acting on the solid phase by the liquid phase can be calculated by integrating the third equation of Eq. (7) over the whole solid surface as

$$\mathbf{F}_{\mathrm{fp}}^{\mathrm{c}} \quad \int_{\Gamma_s} \mathbf{t}_{\Gamma_s}\, dS. \tag{8}$$

The surface integral can be transformed to a volume integral using the divergence theorem which leads to

$$\int_{\Gamma_s} \mathbf{t}_{\Gamma_s}\, dS \quad \int_{\Gamma_s} \boldsymbol{\Sigma}\cdot\mathbf{n}\, dS \quad \int_{\Omega_s} \nabla\cdot\boldsymbol{\Sigma}\, dV. \tag{9}$$

The total stress tensor $\boldsymbol{\Sigma}$ in Eq. (9) consists of two terms given by

$$\boldsymbol{\Sigma} \quad p\mathbf{I} + \boldsymbol{\tau}, \tag{10}$$

where p is the pressure and $\mathbf{I}$ the identity tensor of size 3×3, while $\boldsymbol{\tau}$ is the viscous stress tensor. For incompressible Newtonian fluids, $\boldsymbol{\tau}$ is deviatoric and given by

$$\boldsymbol{\tau} \quad \mu\left(\nabla\mathbf{U} + (\nabla\mathbf{U})^{\mathrm{T}}\right). \tag{11}$$

Substituting Eqs. (9)–(11) into Eq. (8), the interaction force acting on the solid phase can be calculated by

$$\begin{aligned} \mathbf{F}_{\mathrm{fp}}^{\mathrm{c}} \quad & \int_{\Omega_s} \nabla\cdot\boldsymbol{\Sigma}\, dV \\ & \int_{\Omega_s} \nabla\cdot\left[\quad p\mathbf{I} + \mu\left(\nabla\mathbf{U} + (\nabla\mathbf{U})^{\mathrm{T}}\right)\right] dV \\ & \int_{\Omega_s} \underbrace{\nabla\cdot(\ p\mathbf{I})}_{\nabla p} + \nabla\cdot\left[\mu\left(\nabla\mathbf{U} + (\nabla\mathbf{U})^{\mathrm{T}}\right)\right] dV. \end{aligned} \tag{12}$$

As derived in the literature (Rusche, 2003), for incompressible Newtonian fluids, the divergence of the viscous stress tensor is given by

$$\nabla\cdot\boldsymbol{\tau} \quad \nabla\cdot\left[\mu\left(\nabla\mathbf{U} + (\nabla\mathbf{U})^{\mathrm{T}}\right)\right] \quad \nabla\cdot(\mu\nabla\mathbf{U}) + \nabla\mathbf{U}\cdot\nabla\mu. \tag{13}$$

In this work, one assumption is that the dynamic viscosity μ defined by the one field formulation ($\mu \quad \alpha_1\mu_1 + (1 \quad \alpha_1)\mu_2$ with α_1 and μ_1 being the volume fraction and dynamic viscosity of phase 1, respectively) is constant, and thus Eq. (13) leads to

$$\nabla\cdot\boldsymbol{\tau} \quad \nabla\cdot\left[\mu\left(\nabla\mathbf{U} + (\nabla\mathbf{U})^{\mathrm{T}}\right)\right] \quad \mu\nabla^2\mathbf{U}. \tag{14}$$

Substituting Eq. (14) into Eq. (12), leads to

$$\begin{aligned} \mathbf{F}_{\mathrm{fp}}^{\mathrm{c}} \quad & \int_{\Omega_s} \nabla\cdot\left[\quad p\mathbf{I} + \mu\left(\nabla\mathbf{U} + (\nabla\mathbf{U})^{\mathrm{T}}\right)\right] dV \\ & \int_{\Omega_s} \left(\quad \nabla p + \mu\nabla^2\mathbf{U}\right) dV. \end{aligned} \tag{15}$$

The volume integral in Eq. (15) can be approximated by summarizing $\nabla p + \mu\nabla^2\mathbf{U}$ at cell centres of all the cells either partially or fully covered by a solid particle as

$$\mathbf{F}_{\mathrm{fp}}^{\mathrm{c}} \approx \sum_{i\ 1}^{N_c} (\ \nabla p + \mu\nabla^2\mathbf{U})V_c, \tag{16}$$

where N_c is the total number of cells, and V_c is the cell volume.

Similarly, the torque $\mathbf{M}_{\mathrm{fp}}^{\mathrm{c}}$ acting on particles by the liquid phase can be calculated by

$$\mathbf{M}_{\mathrm{fp}}^{\mathrm{c}} \quad \int_{\Gamma_s} \mathbf{r}\times\mathbf{t}_{\Gamma_s}\, dS \quad \int_{\Omega_s} \mathbf{r}\times(\ \nabla p + \nabla\cdot\boldsymbol{\tau})\, dV, \tag{17}$$

where $\mathbf{r}$ is the position vector. $\mathbf{M}_{\mathrm{fp}}^{\mathrm{c}}$ is approximated by summarizing all these quantities as

$$\mathbf{M}_{\mathrm{fp}}^{\mathrm{c}} \approx \sum_{i\ 1}^{N_c} \mathbf{r}\times\left(\quad \nabla p + \mu\nabla^2\mathbf{U}\right)V_c. \tag{18}$$

The last terms on the right hand side of Eqs. (5) and (6) are due to the capillary interactions among particles protruding from the free surface of liquids. The capillary force is of great importance for surface tension dominant flow because capillary interactions govern the motions, leading to self assembly or self organization of

particles which appear at a free surface (Fujita, Koike, & Yamaguchi, 2013). The capillary force is a long range attractive force which is more dominant than other forces, e.g. inertial force and gravita tional force for surface tension dominant cases (Uzi, Ostrovski, & Levy, 2016). Thus, this force is accounted for in this work.

As proven by Fujita et al. in the literature (Fujita et al., 2013), the sum of the surface tension force along the three phase contact line ∂s is equal to the sum of the surface tension force over the virtual free surface fully immersed inside the solid particle in three di mensions as shown in Fig. 3.

The immersed free surface model proposed in the literature (Fujita, Koike, & Yamaguchi, 2015; Nguyen et al., 2021; Washino et al., 2023) is extended to account for the wettability of solid particles at a free surface in this work. The basic idea is to solve the extrapolation equation

$$\frac{\partial \alpha_l}{\partial t} + \mathbf{t}_e \cdot \nabla \alpha_l \quad 0 \tag{19}$$

in the true particle domain, namely, a domain with $\epsilon_f < 0.5$ to extrapolate the free surface from the liquid phase inside solid particles (Nguyen et al., 2021). In Eq. (19), $\mathbf{t}_e$ is the tangent vector to the liquid surface pointing towards the particle. It is used to extend the liquid volume fraction and is defined by

$$\mathbf{t}_e \quad \frac{\mathbf{n}_s \quad (\mathbf{n}_e \cdot \mathbf{n}_s)\mathbf{n}_e}{|\mathbf{n}_s \quad (\mathbf{n}_e \cdot \mathbf{n}_s)\mathbf{n}_e|} \tag{20}$$

with $\mathbf{n}_e$ being the normal vector to the liquid pointing inside the liquid, which is given by

$$\mathbf{n}_e \quad \mathbf{n}_s \cos\theta + \mathbf{t}_s \sin\theta. \tag{21}$$

Here θ is the contact angle between the surface of the solid particle and the free surface. The normal vector to the particle surface pointing inwards $\mathbf{n}_s$ and the unit vector $\mathbf{t}_s$ perpendicular to $\mathbf{n}_s$ are defined by

$$\mathbf{n}_s \quad \frac{\nabla \epsilon_s}{|\nabla \epsilon_s|} \tag{22}$$

and

$$\mathbf{t}_s \quad \frac{\nabla \alpha_l \quad (\mathbf{n}_s \cdot \nabla \alpha_l)\mathbf{n}_s}{|\nabla \alpha_l \quad (\mathbf{n}_s \cdot \nabla \alpha_l)\mathbf{n}_s|}, \tag{23}$$

respectively, where ϵ_s is the solid fraction defined by 1.0 ϵ_f.

In addition to the extrapolation equation given by Eq. (19), another model proposed by Fujita et al. (Fujita et al., 2015) is also implemented in this work. The first model given by Eq. (19) is named as *Model A* and the other model is called *Model B*. The extrapolation equation of *Model B* is given by

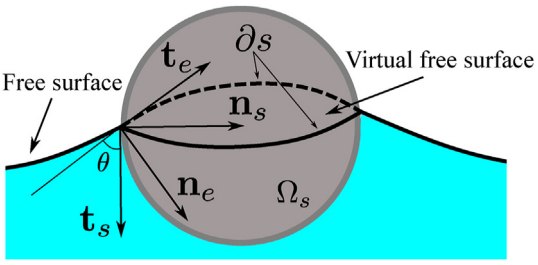

Fig. 3. The schematic diagram of the capillary force model. The virtual free surface is bounded by the solid and dashed three-phase contact lines ∂s.

$$\frac{\partial \alpha_l}{\partial t} + \epsilon_s \mathbf{n}_s \cdot \nabla \alpha_l \quad \epsilon_s |\nabla \alpha_l| \cos\theta. \tag{24}$$

Solving a diffusion equation and then an anti diffusion equation to smoothen the liquid volume fraction field α_l and simultaneously suppressing the interface diffusion after solving Eq. (19) or Eq. (24) to guarantee more numerical stability was proposed by Nguyen et al. (Nguyen et al., 2021). In this work, a simple approach without interface diffusion is applied, namely, the Laplacian filter approach proposed by Lafaurie et al. (Lafaurie, Nardone, Scardovelli, Zaleski, & Zanetti, 1994) is adopted to transform $\mathbf{t}_e \cdot \nabla \alpha_l$ in Eq. (19) or $\mathbf{n}_s \cdot \nabla \alpha_l$ in Eq. (24) into a smoother function $\mathbf{t}_e \cdot \widetilde{\nabla} \alpha_l$ or $\mathbf{n}_s \cdot \widetilde{\nabla} \alpha_l$. The transformations for $\mathbf{t}_e \cdot \nabla \alpha_l$ and $\mathbf{n}_s \cdot \nabla \alpha_l$ are given by

$$\mathbf{t}_e \cdot \widetilde{\nabla} \alpha_l \quad \frac{\sum_f^n {}_1 (\mathbf{t}_e \cdot \nabla \alpha_l)_f S_f}{\sum_f^n {}_1 S_f}, \tag{25}$$

$$\mathbf{n}_s \cdot \widetilde{\nabla} \alpha_l \quad \frac{\sum_f^n {}_1 (\mathbf{n}_s \cdot \nabla \alpha_l)_f S_f}{\sum_f^n {}_1 S_f}, \tag{26}$$

respectively, where S_f is the magnitude of the fth face area of the computational cell which is bounded by n faces, and f denotes the face index. The value of $(\mathbf{t}_e \cdot \nabla \alpha_l)_f$ or $(\mathbf{n}_s \cdot \nabla \alpha_l)_f$ at the face centre is calculated using linear interpolation over the interface region. The smooth function is then used to solve either Eq. (19) or Eq. (24) to construct a smooth virtual free surface. An artificial correction of the liquid volume fraction field α_l given by

$$\alpha_l \quad \max(0, \min(1, \alpha_l)) \tag{27}$$

after solving, Eq. (19) or Eq. (24) is conducted to guarantee the boundedness of α_l. Artificial boundedness of the liquid volume fraction field inside the solid phase by Eq. (27) leads to mass con servation issues, namely, the total liquid volume in the whole computational domain is not conserved. A numerical correction step is then adopted to correct the liquid volume fraction in the liquid phase. First, the total liquid volume of the pure liquid phase before solving Eq. (19) or Eq. (24) denoted as V_{before} is calculated by

$$V_{\text{before}} \quad \int_\Omega \epsilon_f \alpha_l \, dV. \tag{28}$$

Second, the total liquid volume of the pure liquid phase after solving Eq. (19) or Eq. (24) denoted as V_{after} is calculated by

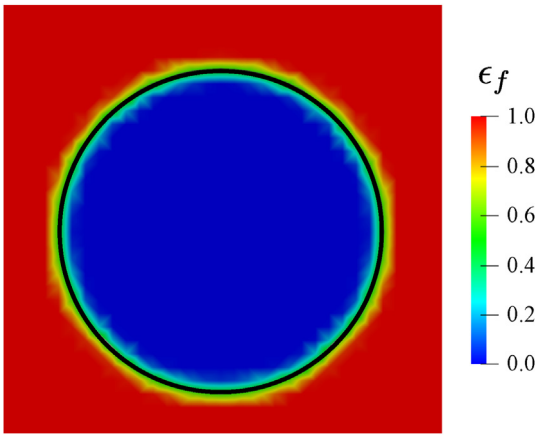

Fig. 4. The void fraction field of a solid particle and the solid black curve represents the iso-surface with ϵ_f 0.5.

$$V_{\text{after}} \quad \int_{\Omega} \epsilon_f \alpha_l \, dV. \tag{29}$$

The volume loss of the pure liquid phase due to the evaporation V_{evap} is calculated by

$$V_{\text{evap}} \quad \int_{\Omega} \frac{\dot{m}}{\rho_l} \Delta t \, dV, \tag{30}$$

where Δt is the time step, and ρ_l is the density of the liquid phase. Accordingly, the volume change ΔV is computed by

$$\Delta V \quad V_{\text{after}} \quad V_{\text{before}} \quad V_{\text{evap}}. \tag{31}$$

The liquid volume fraction field α_l in the liquid phase ($\epsilon_f > 0.5$) can be corrected by

$$\alpha_l \quad \alpha_l + \frac{\epsilon_f \Delta V |\nabla \alpha_l|}{S_s}. \tag{32}$$

Here S_s is the total surface area of the pure liquid phase calculated by

$$S_s \quad \int_{\Omega} \epsilon_f |\nabla \alpha_l| \, dV. \tag{33}$$

The numerical procedure to construct the virtual free surface inside solid particles using the Immersed Free Surface model is outlined as follows:

- Smoothening either $\mathbf{t}_e \cdot \nabla \alpha_l$ with Eq. (25) or $\mathbf{n}_s \cdot \nabla \alpha_l$ with Eq. (26) before solving Eq. (19) for *Model A* and Eq. (24) for *Model B*, respectively.
- Solving either Eq. (19) or Eq. (24) to construct a virtual free surface inside solid particles.
- Using Eq. (27) to correct and constrain the liquid volume frac tion field α_l, artificially.
- Correcting the liquid volume fraction in the liquid phase with Eq. (32).

Once constructing the virtual free surface inside solid particles as shown in Fig. 3, the capillary force can be calculated by

$$\mathbf{F}_{\text{cp}} \quad \oint_{\partial s} \sigma K \mathbf{n} \, ds, \tag{34}$$

where ds is the infinitesimal integration area, and σ and K are the surface tension coefficient and mean interface curvature, respec tively. As derived in Appendix B of (Tryggvason, Scardovelli, & Zaleski, 2011), the surface integral over the immersed free surface S in Eq. (34) can be transformed into a volume integral enclosing the immersed free surface S shown in Fig. 3 given by

$$\mathbf{F}_{\text{cp}} \quad \int_{\Omega_s} \sigma K \mathbf{n} \delta_s \, dV, \tag{35}$$

where δ_s is a Dirac function (Tryggvason et al., 2011). The term $\sigma K \mathbf{n} \delta_s$ can be can be summarized as the surface tension force $\mathbf{F}_{\text{st}}$. As suggested in the literature (Nguyen et al., 2021), the capillary force can then be calculated over the true particle domain, namely domain with $\epsilon_f < 0.5$ (see Fig. 4) by

$$\mathbf{F}_{\text{cp}} \quad \int_{\Omega_s^{\epsilon_f < 0.5}} \mathbf{F}_{\text{st}} \, dV. \tag{36}$$

Similarly, the torque resulting from the capillary force can be calculated by

$$\mathbf{M}_{\text{cp}} \quad \int_{\Omega_s^{\epsilon_f < 0.5}} \mathbf{r} \times \mathbf{F}_{\text{st}} \, dV, \tag{37}$$

once the surface tension force $\mathbf{F}_{\text{st}}$ is known.

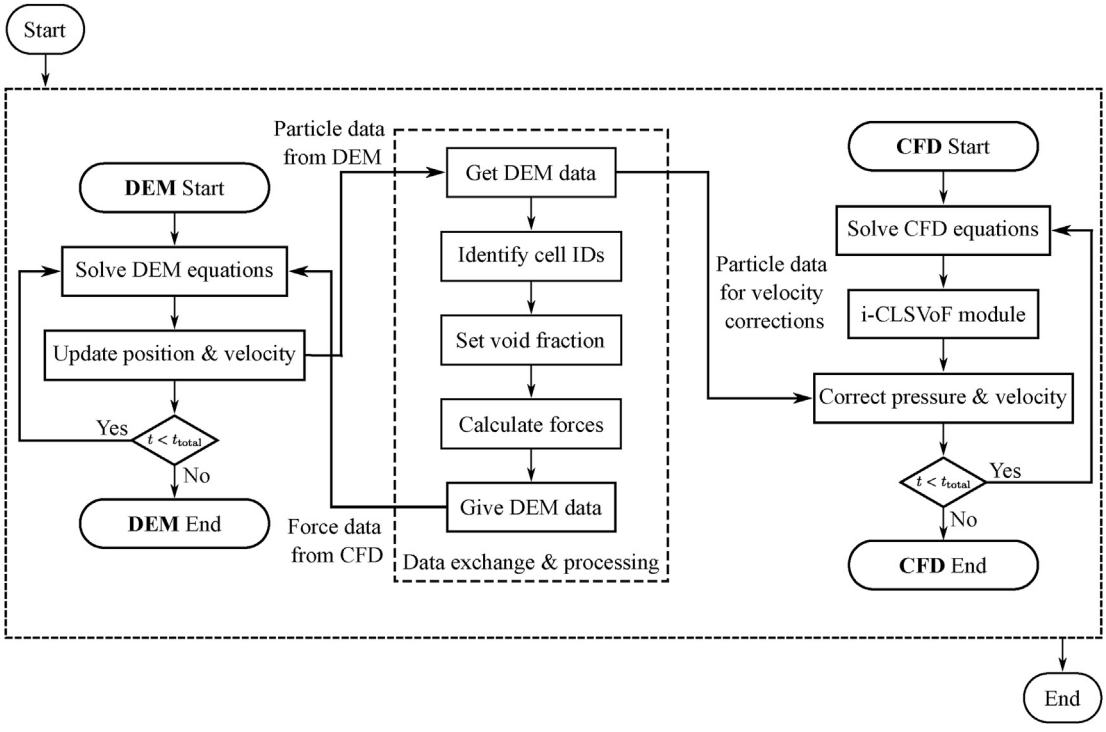

Fig. 5. The coupling algorithm for the resolved CFD-DEM approach.

However, some preliminary numerical simulations demonstrate that this approach suffers from un physical spurious velocities in side solid particles, which is also discussed in the literature (Washino et al., 2023). Therefore, the filtered surface tension force model implemented and discussed in our previous work (Xia & Kamlah, 2024) is adopted here to calculate the capillary force and the torque as

$$\mathbf{F}_{\mathrm{cp}} \quad \int_{\Omega_s^{\epsilon_f<0.5}} \mathbf{F}_{\mathrm{st},f}^{f}\, dV \tag{38}$$

and

$$\mathbf{M}_{\mathrm{cp}} \quad \int_{\Omega_s^{\epsilon_f<0.5}} \mathbf{r}\times\mathbf{F}_{\mathrm{st},f}^{f}\, dV, \tag{39}$$

respectively, where $\mathbf{F}_{\mathrm{st},f}^{f}$ is the filtered surface tension force.

Alternatively, the term $\mathbf{F}_{\mathrm{st}}$ in Eqs. (36) and (37) can be replaced by $\mathbf{F}_{\mathrm{ccf}}$ calculated by the Continuous Capillary Force (CCF) model (Washino, Tan, Hounslow, & Salman, 2013) which is given by

$$\mathbf{F}_{\mathrm{ccf}} \quad \sigma\mathbf{t}_c(\nabla\alpha_l\cdot\mathbf{t}_s)(\nabla\epsilon_s\cdot\mathbf{n}_s), \tag{40}$$

where $\mathbf{t}_c$ is given by

$$\mathbf{t}_c \quad \frac{\mathbf{n}_s \quad (\mathbf{n}_c\cdot\mathbf{n}_s)\mathbf{n}_c}{|\mathbf{n}_s \quad (\mathbf{n}_c\cdot\mathbf{n}_s)\mathbf{n}_c|}. \tag{41}$$

In the resolved CFD DEM approach, one solid particle covers several CFD cells, and thus, the void fraction ϵ_f is of great impor tance in calculating $\mathbf{F}_{\mathrm{fp}}^{c}$, $\mathbf{M}_{\mathrm{fp}}^{c}$ and some other quantities, accurately. The smooth representation algorithm proposed by Hager (Hager, 2014) is used in this paper to create a smooth transition of the void fraction around the particle surface. It is proven that this al gorithm is more stable than the conventional stair step represen tation algorithm (Hager, 2014) and guarantees reasonable numerical accuracy.

3.2. The numerical procedure

In literature, an additional force term is incorporated to the right hand side of the momentum Eq. (2) to account for the interaction force acting on the fluid phase by the solid phase, which is known as the direct forcing approach (Balachandran Nair et al., 2021; Uhlmann, 2005; Washino et al., 2023; Wu, Peters, Rosemann, & Kruggel Emden, 2020). Instead of this, the numeri cal correction approach proposed in the literature as well (Hager, 2014; Hager et al., 2014; Podlozhnyuk, 2018) is used in the cur rent work. The numerical procedure to solve these equations mentioned above within the resolved CFD DEM framework and the numerical correction step to guarantee the divergence free condi tion of the velocity field are detailed below:

- First, an intermediate velocity field $\widehat{\mathbf{U}}$ is solved from the Navier Stokes equations (Eqs. (1) and (2)) over the whole computa tional domain. In this step, the presence of solid particles in the CFD domain is not considered.
- Second, the intermediate velocity field $\widehat{\mathbf{U}}$ in the CFD cells covered by a solid particle is overwritten by imposing the par ticle velocity calculated from the DEM side, explicitly. This leads to a new velocity field $\widetilde{\mathbf{U}}$.
- In general, the new velocity field $\widetilde{\mathbf{U}}$ is not divergence free. Thus, a numerical correction step is further needed to correct this velocity. A Poisson equation given by

$$\nabla^2\varphi_r \quad \nabla\cdot\widetilde{\mathbf{U}} \quad \epsilon_f\dot{m}\left(\frac{1}{\rho_g} \quad \frac{1}{\rho_l}\right) \tag{42}$$

is solved for the velocity potential field φ_r. Another new velocity from numerical correction is defined as $\mathbf{U}$ given by

$$\mathbf{U} \quad \widetilde{\mathbf{U}} \quad \nabla\varphi_r. \tag{43}$$

It can be proven that the new velocity field $\overline{\mathbf{U}}$ is divergence free:

$$\begin{aligned}\nabla\cdot\mathrm{U} \quad \nabla\cdot(\widetilde{\mathrm{U}} \quad \nabla\varphi_r) \quad \nabla\cdot\widetilde{\mathrm{U}} \quad \underbrace{\nabla\cdot\nabla\varphi_r}_{\nabla^2\varphi_r}\\ \nabla\cdot\widetilde{\mathrm{U}} \quad \nabla\cdot\widetilde{\mathrm{U}} + \varepsilon_f\dot{m}\left(\frac{1}{\rho_g} \quad \frac{1}{\rho l}\right)\\ \varepsilon_f\dot{m}\left(\frac{1}{\rho_g} \quad \frac{1}{\rho l}\right).\end{aligned} \tag{44}$$

Here the last term $\epsilon_f\dot{m}(\frac{1}{\rho_g} \quad \frac{1}{\rho_l})$ in Eqs. (42) and (44) results from the phase change of the liquid phase which is equal to zero when there is no phase change.

- The velocity potential field φ_r is also used to correct the pressure field by

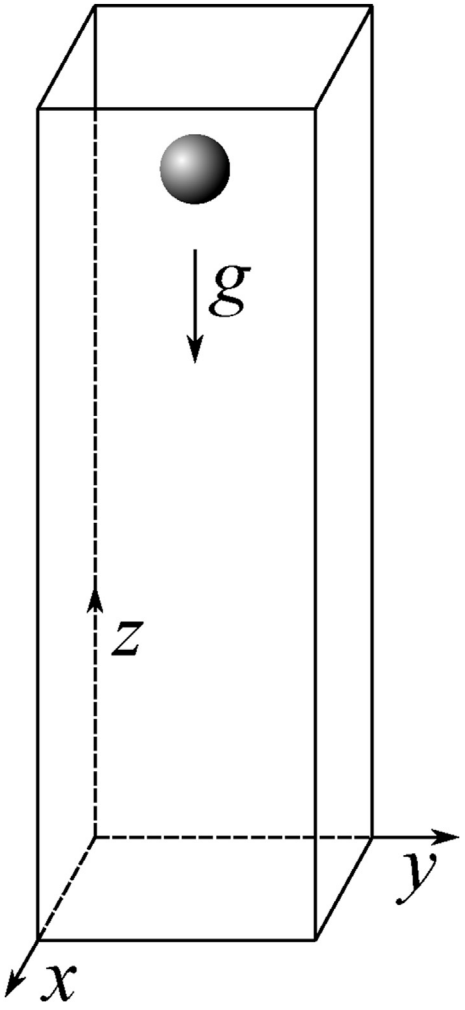

Fig. 6. The schematic diagram of the numerical set-up for calculations of the drag coefficient.

Table 2
Parameters for numerical simulations used to validate calculations of the drag coefficient.

Parameter	Value [unit]
Domain size (length, width, height)	(20, 20, 60) [mm]
Particle diameter	2 [mm]
Particle density	3000 [kg/m^3]
Liquid density	1000 [kg/m^3]
Initial particle position (x, y, z)	(10, 10, 50.5) [mm]

$$p \quad \widehat{p} + \rho \frac{\varphi_r}{\Delta t}, \tag{45}$$

where $\widehat{p}$ is the pressure field solved from the Navier Stokes equations (Eqs. (1) and (2)), ρ is the density field and Δt the time step.

3.3. Coupling algorithm

The open source framework CFDEMcoupling PUBLIC (D. Computing and CFDEM®coupling, 2017) is extended to implement the variable−density based multiphase framework coupling CFD to DEM. A new coupling solver named cfdemSolverVoFIB based on the standard solver cfdemSolverIB of the CFDEMcoupling PUBLIC library is developed in this paper. The cfdemSolverIB solver is not capable of modelling variable−density incompressible flow with surface tension and evaporation. Accordingly, the extended solver cfdemSolverVoFIB is developed in this work. The new solver is capable of realizing the following functionality:

- Get particle data, e.g. particle coordinates, velocity and particle radius from DEM.
- Identify CFD cells covered by solid particles and calculate the void fraction ϵ_f of each CFD cell.
- Correct the velocity field when solid particles are present in the liquid phase.
- Calculate the fluid−solid interaction force and capillary force.
- Give essential data to DEM, e.g. buoyancy, capillary force, fluid−solid interaction force and so on.
- Repeat these steps mentioned above until the simulation ends.

A detailed coupling algorithm between DEM and CFD for the resolved CFD DEM approach is shown in Fig. 5. The solver cfdemSolverVoFIB consists of three modules, namely, the CFD module, the DEM module and the data exchange and processing module as shown in Fig. 5. OpenFOAM and LIGGGHTS are employed to conduct the CFD and DEM simulations, respectively. In the resolved CFD DEM simulations, DEM and CFD conduct their simulations, separately, once the CFD DEM simulation starts. In DEM, the governing equations (Eqs. (5) and (6)) are solved to update the velocity, position and other information for solid particles. This information is transferred to the data exchange and processing module for further calculations as detailed below. In CFD, the governing equations (Eqs. (1) and (2)) are first solved to update an intermediate velocity field, ignoring solid particles present in the liquid phase. The i CLSVoF module detailed in our previous work (Xia & Kamlah, 2024) is used to capture the moving free surface and calculate the surface tension force.

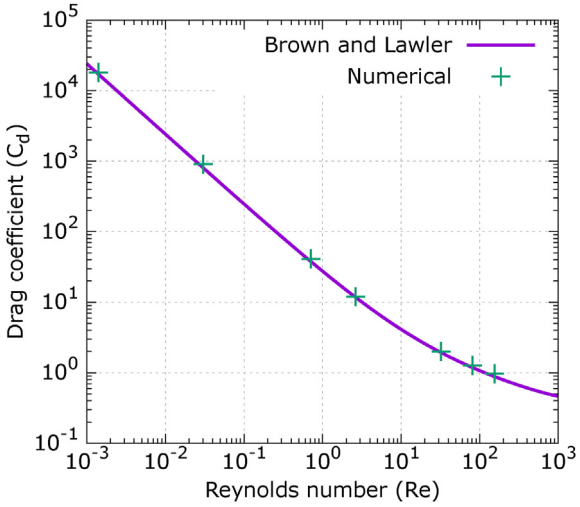

Fig. 7. Validations for calculations of the drag coefficient C_d.

The data exchange between DEM and CFD is crucial to realize the resolved CFD DEM coupling. The essential data, e.g. particle positions and velocities calculated on the DEM side, are transferred to the data exchange and processing module. Then, the CFD cells covered by solid particles can be identified, and the void fraction for these CFD cells can be obtained. Furthermore, the particle−fluid interaction forces can be calculated in the data processing module and then transferred to the DEM side to update particle data in the next cycle. Particle velocity data from DEM are transferred to the CFD side, and the numerical correction step is then used to correct the velocity field to satisfy the divergence free condition as discussed in Section 3.2.

The time step size for stable DEM simulations is given by the Rayleigh time step given by

$$\Delta t^{\mathrm{DEM}} \quad f_s \frac{\pi R \sqrt{\frac{2\rho(1+\nu)}{Y}}}{0.1631\nu + 0.8766}, \tag{46}$$

where R is the average particle radius, ρ the particle density, Y the Young's modulus and ν the Poisson's ratio (Li, Xu, & Thornton, 2005). Additionally, f_s is a safety factor for which a value ranging from 0.1 to 0.3 is recommended. The maximum time step for guaranteeing a stable CFD simulation is given by two constrains. The first constraint is

$$\Delta_{t\sigma} < \sqrt{\frac{\rho_{\mathrm{avg}} \Delta x^3}{2\pi\sigma}}, \tag{47}$$

where ρ_{avg} is the average density of the phases. It is proposed for the explicit treatment of the surface tension force term (Brackbill, Kothe, & Zemach, 1992). Another more comprehensive time step constraint is given by

$$\Delta_{tc} < \frac{1}{2}\left(C_2\tau_\mu + \sqrt{(C_2\tau_\mu)^2 + 4C_1\tau_\rho{}^2}\right), \tag{48}$$

Table 3
Dynamic viscosities for these seven different cases.

Case No.	1	2	3	4	5	6	7
μ [Pa s]	2.5	5×10^{-1}	1×10^{-1}	5×10^{-2}	1×10^{-2}	5×10^{-3}	3×10^{-3}

Table 4
Terminal velocity and relative error for these seven validation cases.

Re [ ]	Terminal velocity [m/s]	C_d Num [ ]	C_d Exp [ ]	Relative error [ ]
0.0014	0.0017	18103.8062	17172.1450	0.0543
0.0304	0.0076	905.8172	800.4452	0.1316
0.7120	0.0356	41.2827	37.7199	0.0945
2.6400	0.0660	12.0110	11.7323	0.0238
32.3600	0.1618	1.9985	1.9306	0.0352
81.2000	0.2030	1.2696	1.1848	0.0716
154.4667	0.2317	0.9746	0.8837	0.1029

Table 5
Parameters for the single particle settling simulations (data adopted from (Ten Cate et al., 2002)).

Case No.	Re [ ]	Liquid density [kg/m^3]	Dynamic viscosity [Pa s]
1	1.5	970	0.373
2	4.1	965	0.212
3	11.6	962	0.113
4	31.9	960	0.058

which involves the density and the viscosity of the multiphase system. τ_μ and τ_ρ are given as $\mu_{\text{avg}}\Delta x/\sigma$ and $\sqrt{\rho_{\text{avg}}\Delta x^3/\sigma}$, respectively, with μ_{avg} being the average dynamic viscosity of the liquid and gas phases (Galusinski & Vigneaux, 2008). Accordingly, the maximum time step size for stable CFD simulations is given as

$$\Delta t^{\text{CFD}} < \min(\Delta_{t\sigma}, \Delta_{tc}) C_{\Delta t} \tag{49}$$

with $C_{\Delta t}$ being the stabilization factor where a range of $C_{\Delta t}$ between 0.3 and 0.7 is recommended for more stable calculation.

The minimal coupling interval for data exchange between DEM and CFD is defined by

$$i_c \quad \frac{\Delta t^{\text{CFD}}}{\Delta t^{\text{DEM}}}, \tag{50}$$

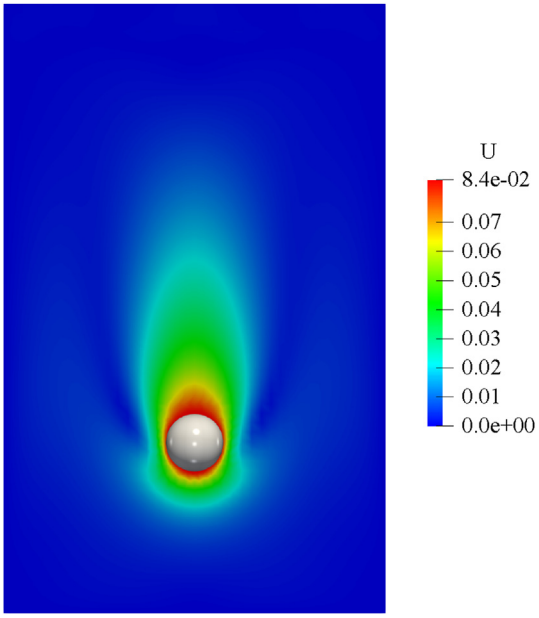

Fig. 8. The liquid velocity field of single particle settling simulation (Re 11.6).

which must be an integer. Increasing the coupling interval requires less computational cost; however, the coupled simulations may then not be accurate enough as the latest data are not exchanged between DEM and CFD in time. The particle data from DEM are used to calculate the void fraction, fluid structure interaction force and so on. These interaction forces are given back to DEM, and thus, the interaction forces acting on the solid phase by the fluid phase can be obtained. DEM and CFD go to the next loop once one data exchange is completed, and the whole simulation ends until the prescribed total simulation time is reached.

4. Results and discussion

4.1. Numerical validation

In this section, three benchmark cases are used to validate the resolved CFD DEM solver cfdemSolverVoFIB developed in this work. The first case compares the drag coefficient calculated with the resolved CFD DEM approach against a formula. The second case is to compare the settling velocities and particle position against the corresponding experimental results when a spherical particle settles in liquids. The last case compares our numerical results of the drafting kissing tumbling of two settling spheres against the corresponding results from the literature.

4.1.1. Validation of calculations of the drag coefficient

The schematic diagram for calculating the drag coefficient is shown in Fig. 6. A sphere falls down under the influence of gravity.

The sphere is fully immersed in the liquid of a container, and the essential parameters for the numerical simulations are listed in Table 2. The dynamic viscosity of the liquid in the container significantly influences the sphere's motion, and a wide range of Reynolds numbers can be achieved by varying the liquid dynamic viscosity. Seven numerical benchmark cases with different dynamic viscosities (refer to Table 3) are conducted in this section.

The motion of a single sphere inside the container is governed by Newton's second law of motion given by

$$m\frac{d\mathbf{U}}{dt} \quad \mathbf{F}_g \quad \mathbf{F}_b \quad \mathbf{F}_d, \tag{51}$$

where $\mathbf{F}_g$, $\mathbf{F}_b$ and $\mathbf{F}_d$ are the gravitational force, buoyancy and drag force acting on the sphere, respectively (Norouzi, Zarghami, Sotudeh Gharebagh, & Mostoufi, 2016). Substituting expressions of these force terms into Eq. (51), leads to

$$\frac{\pi\rho_p D_p^3}{6}\frac{d\mathbf{U}}{dt} \quad \frac{\pi(\rho_p \quad \rho_f)D_p^3\mathbf{g}}{6} \quad \frac{1}{8}C_d\pi D_p^2\rho_f\mathbf{U}^2, \tag{52}$$

where D_p is the particle diameter, and ρ_p and ρ_f are the density for the solid and liquid phases, respectively.

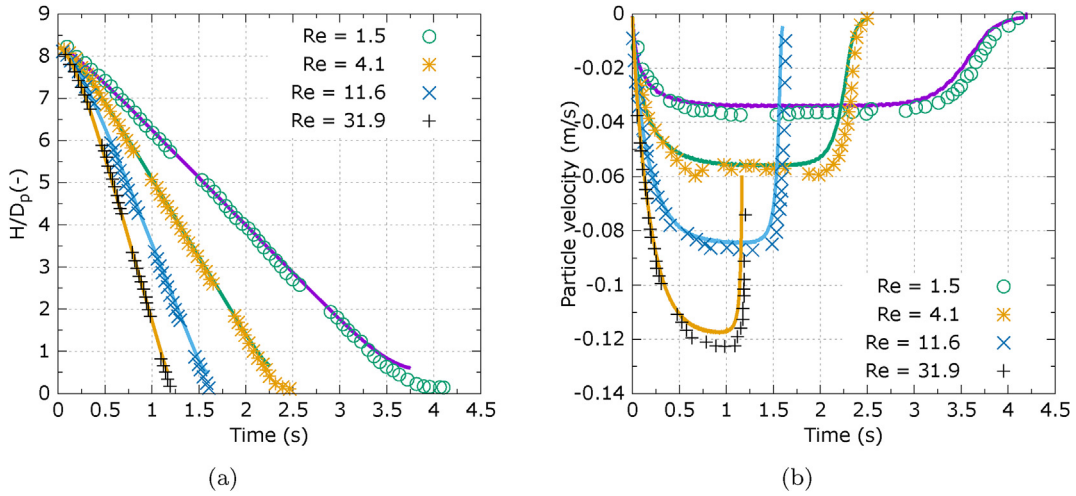

Fig. 9. Validations of the single sphere settling in liquids: (**a**) dimensionless sphere height, (**b**) sphere settling velocity.

Thus, the rate of change of particle velocity **U** with respect to time is given by

$$\frac{d\mathbf{U}}{dt} \quad \frac{3\rho_f C_d}{4\rho_p D_p}\mathbf{U}^2 + \frac{\rho_p \quad \rho_f}{\rho_p}\mathbf{g}. \tag{53}$$

Typically, the particle velocity increases gradually and reaches a steady velocity, known as the terminal velocity, when a particle settles in a fluid. Thus, the drag coefficient C_d in Eq. (53) can be calculated by

$$C_d \quad \frac{4}{3}\frac{\rho_p \quad \rho_f}{\rho_f}\frac{|\mathbf{g}|D_p}{|\mathbf{U}_t|^2}, \tag{54}$$

where $|\mathbf{U}_t|$ is the magnitude of the terminal velocity. Furthermore, the particle Reynolds number is given by

$$\mathrm{Re} \quad \frac{|\mathbf{U}_t|D_p}{\nu}, \tag{55}$$

where ν is the kinematic viscosity of the liquid phase.

$$C_d \quad \frac{24}{\mathrm{Re}}(1.0 + 0.15\mathrm{Re}^{0.681}) + \frac{0.407}{1 + \frac{8710}{\mathrm{Re}}} \tag{56}$$

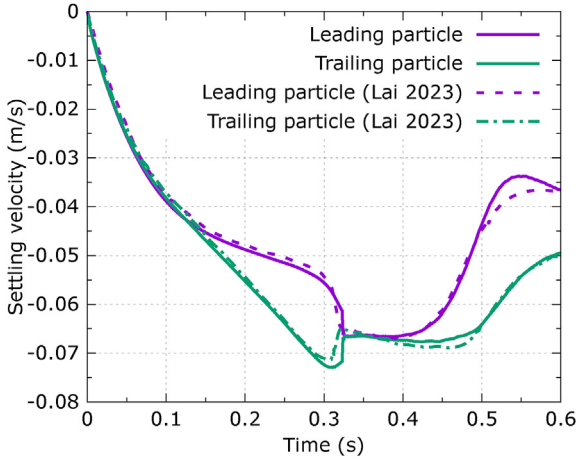

Fig. 10. Validations of the settling velocity for drafting-kissing-tumbling of two particles.

Brown et al. corrected the drag coefficient by comparing the corrected formula against extensive experimental data (Brown & Lawler, 2003). This corrected drag coefficient (denoted as C_d Exp) is used to validate the drag coefficient calculations in this section where the drag coefficient calculated from the numerical simulations (with Eq. (54)) is denoted as C_d Num.

The comparison between the numerical drag coefficient and the corrected drag coefficient given by the formula Eq. (56) is shown in Fig. 7. Good agreement is obtained for a wide range of Reynolds numbers ranging from 10 ^{3} to 10^3. The relative errors of calculating the drag coefficient are listed in Table 4 for the quantitative comparison. Calculations of the drag coefficient are more accurate for the Reynolds number between 0.1 and 100. However, the accuracy of the model needed to be improved for high Reynolds numbers, namely when Re is larger than 100. This relatively large discrepancy for simulations with high Reynolds numbers was reported in the literature as well (Schnorr Filho et al., 2022; Shen et al., 2022).

4.1.2. *Single particle settling in a container*

The experimental study and corresponding numerical simulations of single particle settling in viscous liquids were conducted by Ten Cate et al. (Ten Cate, Nieuwstad, Derksen, & Van den Akker, 2002). The experimental set up for the single particle settling is a spherical bearing ball with a diameter of 15 mm, and a density of 1120 kg/m^3 which settles in a container (length $\times$ width $\times$ height 100 $\times$ 100 $\times$ 160 mm) under the influence of gravity (g 9.81 m/s^2 in the vertical direction). The sphere is fully immersed in the liquid before it starts to fall, and the initial separation distance between the sphere centre and the bottom wall of the container is 120 mm. The sphere experiences acceleration at the beginning and then decelerates when it approaches the bottom wall. This scenario is suitable for validating the numerical implementations for computing the fluid–solid interaction forces and the trajectory of the spherical particle.

In this section, four cases with different liquid densities and dynamic viscosities are considered to validate the numerical model developed in this paper. These essential parameters are detailed in Table 5.

The number of cells of the base mesh resolution is 40 $\times$ 40 $\times$ 64. Adaptive mesh refinement is used to guarantee fine mesh

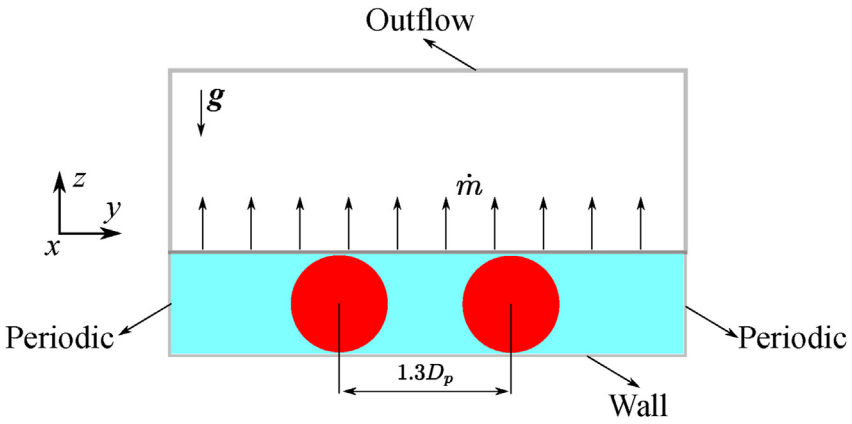

Fig. 11. 2D schematic diagram of the numerical set-up for two particles moving along a free surface with evaporation.

Table 6
Parameters for two particles moving along a free surface with evaporation.

Parameter [unit]	Value
Liquid density [kg/m^3]	10
Gas density [kg/m^3]	1
Particle density [kg/m^3]	25
Particle diameter [m]	1.0×10^{-5}
Liquid viscosity [Pa s]	1.0×10^{-3}
Gas viscosity [Pa s]	1.0×10^{-5}
Surface tension [N/m]	0.072
CFD time step [s]	1.0×10^{-9}
DEM time step [s]	1.0×10^{-9}
Coupling interval [ ]	1
Restitution coefficient [ ]	0.5
Friction coefficient [ ]	0.3
Contact angle (particle-interface) [ ]	30°, 45°, 60°
Contact angle (particle-wall) [ ]	0°

resolution around the sphere and to allow a relatively coarse mesh elsewhere to reduce computational cost while guaranteeing reasonable numerical accuracy. The no slip boundary condition is applied to the boundary of the container. The time step size for both DEM and CFD is 1.0×10^{-5}, and a coupling interval of one is used to exchange data between DEM and CFD.

The liquid velocity field for Re 11.6 is shown in Fig. 8. An elongated wake can be seen from the simulation. The dimension less gap height H/D_p between the sphere and the bottom wall and the magnitude of the particle settling velocity in the vertical di rection are recorded and compared against the corresponding experimental results. The comparison is shown in Fig. 9. Figs. 9(a) and (b) are the dimensionless gap height and article settling ve locity, respectively. The solid curves represent numerical results, while the points represent experimental results adopted from the literature (Ten Cate et al., 2002). As shown in Fig. 9(b), the spherical particle first undergoes an acceleration phase and then decelerates due to squeezing liquid between the sphere and the bottom wall when the particle approaches the bottom wall. A good agreement can be found for these four different cases. Some minor discrepancies can be seen from Fig. 9(a), especially when Re 1.5. The reason is that the lubrication force is not negligible when the gap between the particle and the bottom wall is small. Incorpo rating the lubrication force can be subject to future work which is not included in the current work. Overall, these simulations demonstrate that the numerical implementation for the resolved CFD DEM model is correct and that the model is accurate enough to capture the complex fluid solid interaction and to predict the tra jectory of solid particles.

4.1.3. *Drafting kissing tumbling of two settling spheres*

In this section, another well known benchmark case is adopted to validate the performance of our improved CFD DEM model. The drafting kissing tumbling of two equal particles has been widely used in the literature (Breugem, 2012; Gong, Wu, An, Zhang, & Fu, 2023; Hager, 2014; Lai, Zhao, Zhao, & Huang, 2023). In contrast to the previous validations with only one particle involved in the numerical simulations, the interactions between two particles in this case bring more numerical difficulties in predicting the particle liquid interaction accurately. Accordingly, this case is suitable for validating the accuracy of our CFD DEM model in dealing with more complicated interactions in resolved CFD DEM simulations.

A computational domain with dimensions of length × width × height $10 \times 10 \times 40$ mm is used for numerical simulations. At t 0, two equal particles with the diameter of 1.67 mm are placed inside the container, and the initial separation distance between them is 3.4 mm. The initial positions of the two particles along the height direction are 31.6 mm and 35 mm, respectively. The upper particle is called the trailing particle, and the other is named the leading particle. The densities of the two particles and the liquid phase are ρ_p 1140 and ρ_l 1000 kg/m^3, respectively. The dynamic viscosity of the liquid phase is 0.001 Pa ·s. The two particles settle under the influence of gravity with the gravitational acceleration g 9.81 m/s^2 along the vertical direction.

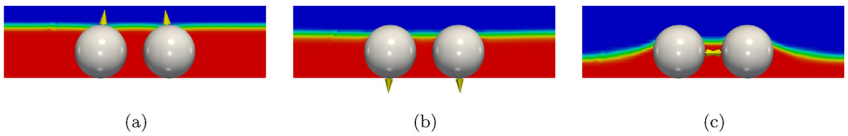

Fig. 12. Vectors of the particle velocity are represented by the yellow arrows during the evaporation process: (a) pointing upwards, (b) pointing downwards, (c) pointing towards each other. (For interpretation of the references to colour in this figure legend, the reader is referred to the Web version of this article.)

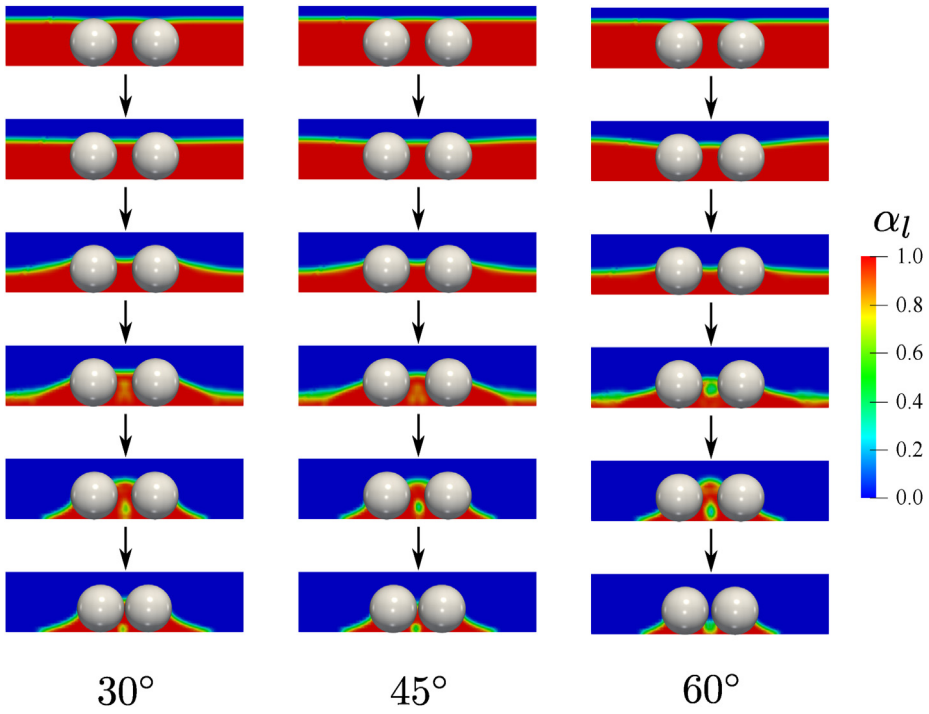

Fig. 13. Numerical simulations of two particles moving along the free surface for three different specified contact angles.

As shown in Fig. 10, the numerical results in predicting the settling velocities of the two particles agree well with the corre sponding data adopted from the literature (Lai et al., 2023). How ever, there is some minor discrepancy regarding the settling velocity when two particles approach and contact with each other. It is due to the potential errors of the volume fraction based resolved CFD DEM approach as discussed in the literature (Lai et al., 2023).

4.2. Application

The improved resolved CFD DEM model developed in this work can be used to model capillary force induced or evaporation induced transport and agglomeration of particles. In this section, two numerical benchmark cases are presented to demonstrate the performance of the resolved CFD DEM model with the capillary interactions developed in this paper.

4.2.1. Two particles moving along a free surface with evaporation

The first simulation is to model the evaporation induced deformation of the meniscus between two spherical particles sitting on a substrate. The numerical set up for the 3D simulation is shown in Fig. 11, namely, two spherical particles resting on a wettable substrate. In Fig. 11, we only show the cross section of the numerical set up by slicing the 3D domain in the x direction for better visualization of the numerical configuration. The initial dis tance between the centres of the two particles is $1.3D_p$ (particle diameter). Periodic boundary conditions are applied in x and y di rections. The initial liquid height is higher than the particle diam eter. The outflow boundary condition is applied at the top to let vapour leave the domain freely. The constant contact angle and slip boundary conditions are applied on the bottom wall. The specified contact angle between the spherical particle and the liquid surface is 30°, and a constant contact angle specified at the bottom wall is 0°. The constant mass flux evaporation model discussed in our previous work (Xia & Kamlah, 2024) is adopted to model the evaporation of the liquid phase into the gas phase with a constant evaporation rate in this section. To demonstrate the performance of the capillary force model extended in this paper, only the gravita tional force, buoyancy and capillary force are effective, while the particle–liquid interaction force given by Eq. (15) is not considered in the numerical simulation. The particle–liquid interaction force

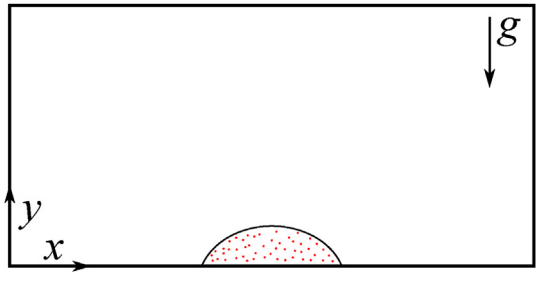

Fig. 14. The schematic diagram of the numerical setup for droplet evaporation with suspended particles.

Table 7
Essential parameters for modelling particle transport inside an evaporating droplet.

Parameter [unit]	Value
Liquid density [kg/m^3]	10
Gas density [kg/m^3]	1
Particle density [kg/m^3]	250
Particle diameter [m]	1.0×10^{-6}
Liquid viscosity [Pa s]	1.0×10^{-3}
Gas viscosity [Pa s]	1.0×10^{-5}
Surface tension [N/m]	0.072
Surface energy density [J/m^2]	0.86×10^{-3}
CFD time step [s]	1.0×10^{-12}
DEM time step [s]	1.0×10^{-12}
Coupling interval [ ]	1
Restitution coefficient [ ]	0.5
Friction coefficient [ ]	0.3
Contact angle (particle-interface) [ ]	30°
Contact angle (particle-wall) [ ]	0°

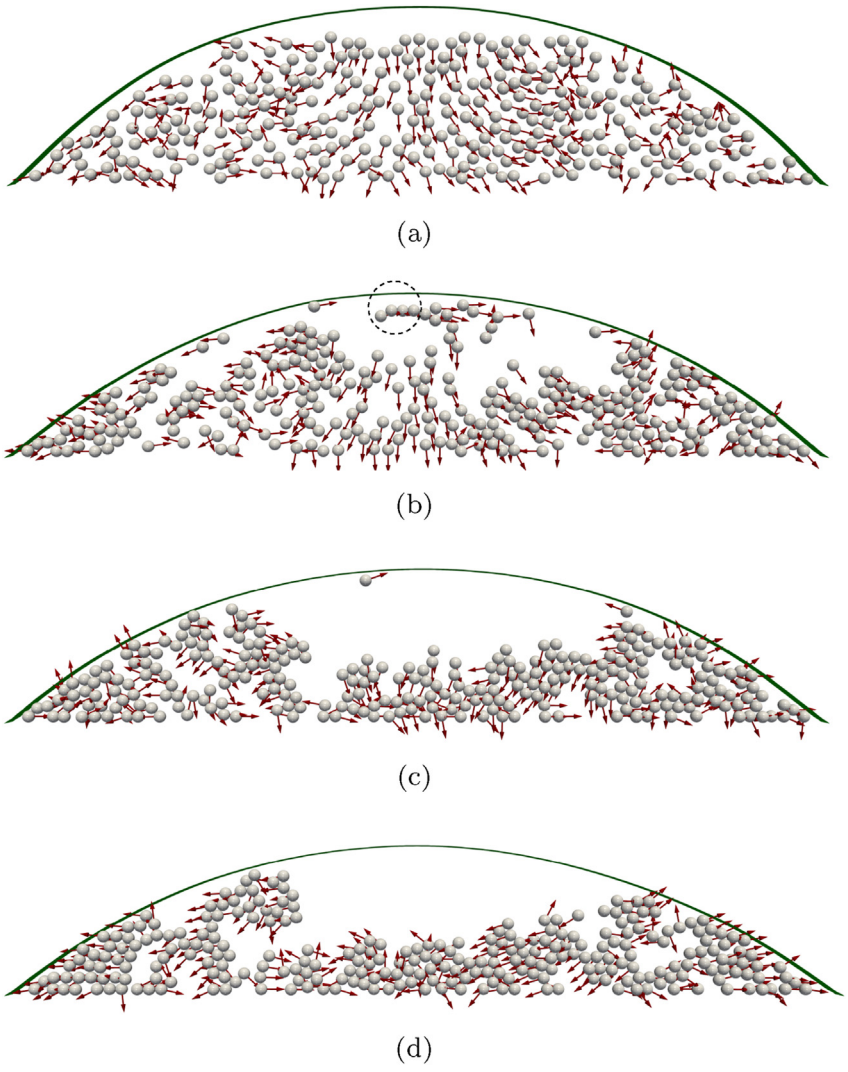

Fig. 15. Snapshots of the numerical simulations of the four stages of particle deposition patterns inside an evaporating droplet.

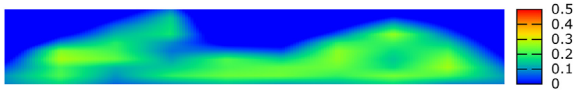

Fig. 16. The local packing fraction for the particle deposition pattern shown in Fig. 15d.

given by Eq. (15) also influences the movements of the two particles during the evaporation process. If this force is active, it is impossible to determine the lateral movement of the two particles due to the capillary force only. The parameters for this simulation are listed in Table 6. In order to speed up the numerical simulations and mitigate the influence of un physical spurious velocities on the internal flow field inside the evaporating droplet, the density of the liquid phase is scaled by 0.01. The density scaled approach is also adopted to model droplet evaporation in the literature (Irfan & Muradoglu, 2017; Ledesma Aguilar, Vella, & Yeomans, 2014; Zhang, Zhang, Zhao, & Yang, 2021).

Table 8
Comparison between the standard cfdemSolverIB solver and the improved solver cfdemSolverVoFIB.

Model/Module	cfdemSolverIB	cfdemSolverVoFIB
Incompressible flow solver	yes	yes
Variable density	no	yes
Free surface capturing	no	yes
Surface tension	no	yes
Capillary force	no	yes
Evaporation of the liquid phase	no	yes

The capillary force is only active when solid particles are partially immersed in liquids. The two particles are fully immersed inside the liquid phase at the beginning of the evaporation, and the capillary force acting on them is zero. The capillary force becomes active when they gradually protrude from the liquid surface and become partially immersed. Two particles gradually protrude from the liquid surface after evaporating some liquid from the liquid surface, as shown in Fig. 12. The vectors of the particle velocity point upwards during the early stage of evaporation (see Fig. 12(a)). This is due to the upward capillary force acting on the two particles when they protrude from the liquid surface. Then, the vectors of the particle velocity point downwards (see Fig. 12(b)) after evaporating more liquid. A concave meniscus be tween the two particles gradually forms, which leads to attractive interactions between them, as shown in Fig. 12(c). This attractive capillary force acting on the two particles makes them moving toward each other.

Three simulations with different contact angles, namely, 30°, 45° and 60° are presented in Fig. 13. The parameters for the solid and liquid phases can be found in Table 6. For the very early stage of evaporation, the free surface gradually decreases due to the mass loss and then contacts with the top of the spheres. The virtual free surface inside the solid particles is concave upward, as shown in the top row of Fig. 13. More mass loss can be found around the two particles when the contact angle increases from 30° to 60°, as shown in the second row of Fig. 13. A concave meniscus and a liquid bridge gradually form around every two particles for the cases with contact angles θ 30° and θ 45°, while a flat meniscus is found for the case with a contact angle of 60°, as shown in the third row of Fig. 13. These concave meniscuses lead to attractive capillary forces and force each pair of particles to come closer to each other. As the simulation continues, more liquid evaporates around two sides of the computational domain, and the shape of the meniscus changes from concave to convex, as demonstrated by the fourth and fifth rows of Fig. 13. In all three cases, particles gradually move towards each other during the evaporation process. The liquid phase evaporates faster when the contact angle increases from 30° to 60°. The same conclusion is also shown in Fig. 4 presented in the liter ature (Mino, Tanaka, Tanaka, Nakaso, & Gotoh, 2022).

4.2.2. Particle transport and accumulation in an evaporating droplet with contact line pinning

In contrast to the aforementioned numerical simulations, the current numerical benchmark case involves many particles in side an evaporating droplet with contact line pinning. In prin ciple, droplet evaporation with contact line pinning results in an internal capillary flow from the droplet centre to the edge (Deegan et al., 1997). The radial capillary flow carries some suspended particles from the droplet centre to its edge and finally leads to an inhomogeneous particle deposition pattern. Accordingly, the internal flow field is of great significance in affecting particle transport and accumulation during the evap oration process. This is in contrast to the first numerical demonstration case as discussed in Section 4.2.1, where capillary force is more dominant, and the internal velocity field does not play a significant role.

In order to save computational cost and to visualize the evaporation induced particle transport during the evaporation process, a simplified numerical simulation is adopted in this sec tion; namely, all the particles inside the evaporating droplet can only move along the x and y directions. The numerical set up is shown in Fig. 14. 300 micro sized spherical particles with a diam eter of 1 μm are generated randomly inside a sessile droplet with an initial contact angle of 45° and a radius of 50 μm. The length and height of the computational domain are 300 μm and 150 μm, respectively. As the particle size is small, the van der Waals force model detailed in the Appendix is incorporated to account for the non contacting attractive force acting on the solid particles during the evaporation process. The parameters used in the simulation are listed in Table 7.

The no slip boundary condition is applied at the bottom wall to fix the contact line during the evaporation process, and the outflow boundary condition is applied at the top to let vapour leave the domain freely. A 2D axisymmetrical model was used in the litera ture (Zhang et al., 2021); however, a non symmetrical numerical configuration with all the particles are randomly distributed inside the sessile droplet, as shown in Fig. 14, is used in this section. The reason is that the initial particle packing for the DEM simulations is not axisymmetric.

Fig. 15 shows snapshots of the numerical simulations. The surface in green represents the free surface of the evaporating droplet. As the evaporation proceeds, the initial contact radius between the sessile droplet and the substrate is constant, and the droplet height decreases gradually. The red arrows indicate the velocity vectors of particles. In the initial stage of the evaporation as shown in Fig. 15(a), particles in the middle of the droplet tend to move downwards, while particles around the two corners tend to move towards the triple contact line region due to the radial capillary flow. As shown in Fig. 15(b), some particles tend to agglomerate with their neighbouring particles around the free surface as highlighted by the dashed circle. More and more par ticles are dragged towards the two corners of the evaporating sessile droplet as the evaporation proceeds, as shown in Fig. 15(c). Fig. 15(d) shows agglomerations of particles around the triple contact line region, while fewer particles are deposited in the middle of the droplet.

In this work, a simple yet helpful approach has been developed to calculate the local packing fraction with the open source Voronoi tessellation code Voro++ (refer to Appendix). This approach is adopted to calculate the local packing structure and packing frac tion for the particle assembly in this section. Fig. 16 shows the local packing fraction for the particle deposition pattern shown in Fig. 15(d). It demonstrates that a higher packing fraction can be found around the two corners where much more particles are agglomerated.

This numerical benchmark case demonstrates that the resolved CFD DEM model can capture the complex particle–fluid, particle–particle and particle–wall interactions when the liquid phase undergoes phase change from liquid to vapour. In experi ments, changing liquid parameters, e.g. the liquid viscosity, was found to alter particle deposition patterns as discussed in the experimental work (Mikolajek et al., 2018). Thus, as inspired by the experimental work, extensive numerical simulations with this resolved CFD DEM model can help to understand the effect of specific parameters on the resulting particle deposition patterns in our future work.

5. Conclusions

In this paper, the theory and numerical issues of the improved resolved CFD DEM approach are discussed. A variable density resolved CFD DEM model is developed, implemented and vali dated. An improved capillary force model has been implemented into the open source CFDEMcoupling PUBLIC library. A corre sponding improved resolved CFD DEM solver cfdemSolverVoFIB has been thus developed. The main contribution and improve ments in this work are as follows:

- A variable density resolved CFD DEM model with sharp free surface capturing has been developed and validated with three well known benchmark cases.
- The evaporation models discussed in our previous work have been incorporated into the cfdemSolverVoFIB solver to model the gas–liquid–solid multiphase system with evaporation of the liquid phase. Numerical demonstrations show the promising applications of the resolved CFD DEM model with evaporation.
- An improved capillary force model with simple yet efficient numerical smoothing has been developed to improve numerical stability issues when modelling capillary interactions for partially floating solid particles moving at a free surface.

A brief comparison between the standard resolved CFD DEM solver cfdemSolverIB implemented in the CFDEMcoupling PUBLIC library and the cfdemSolverVoFIB developed in this work is out lined in Table 8. It turns out that the new solver cfdemSolverVoFIB developed in this paper extends the applications of the standard resolved CFD DEM solver cfdemSolverIB.

Three numerical validation cases have been conducted to vali date the resolved CFD DEM solver developed in this work. It is proven that the resolved CFD DEM solver predicts complex particle–fluid interactions with reasonable numerical accuracy. Two numerical benchmark cases, e.g. two particles moving along a free surface with evaporation and evaporation induced agglomer ations of many particles inside an evaporating droplet, have been presented in this paper. It demonstrates that the performance of the improved resolved CFD DEM solver is reasonably good in modelling gas–liquid–solid multiphase systems.

Declaration of interest

The authors declare that they have no known competing financial interests or personal relationships that could have appeared to influence the work reported in this paper.

Acknowledgements

We sincerely thank the funding from China Scholarship Council (CSC) for the financial support (CSC201808350108), and the Helmholtz Association in Germany. Some simulations were done using the computational source of the BwUniCluster 2.0.

Appendix

The van der Waals force

The van der Waals force serves as an attractive force between two interacting particles or a particle and a wall. The magnitude of the van der Waals force between two particles is related to their respective radius R_i and R_j, separation distance h and the material property defined by the Hamaker constant H_a (Hamaker, 1937). The formula for calculating the van der Waals force between two par ticles is defined by

$$\mathbf{F}_{ij}^{\mathrm{vdw}} \quad \frac{H_a}{6}\frac{64R_i^3R_j^3(h+R_i+R_j)}{(h^2+2R_ih+2R_jh)^2(h^2+2R_ih+2R_jh+4R_iR_j)^2}, \tag{A.1}$$

where the minus sign means that the force is attractive (Yang, Zou, & Yu, 2000). Additionally, the van der Waals force between a par ticle and a wall is given by

$$\mathbf{F}_{\mathrm{pw}}^{\mathrm{vdw}} \quad \frac{H_aR_i}{6h^2}, \tag{A.2}$$

where the magnitude of the force depends on particle radius R_i, the materials property and the separation distance h between the particle and the wall (Abbasfard, Evans, & Moreno Atanasio, 2016). The crucial material property Hamaker constant H_a is related to the surface energy density γ_s and the cutoff distance $h_{\min}$ (Gotzinger & Peukert, 2003). Accordingly, H_a can be calculated by

$$H_a \quad 24\pi\gamma_s h_{\min}^2. \tag{A.3}$$

Furthermore, the separation distance h appears in the denom inator, for which a cutoff distance $h_{\min}$ is defined to avoid numerical singularities when h approaches zero.

Corresponding numerical calculations are conducted to validate the numerical accuracy in computational modelling of the att ractive force due to the presence of the van der Waals force, only. The basic numerical set up is a single particle i approaching another particle j or a fixed wall with an initial separation distance h_0 ($h_0 > 0$) while the van der Waals forces are recorded for the two cases, respectively. The parameters used in the numerical simula tions are outlined in Table A.1. The van der Waals forces collected from the numerical simulations are compared to the analytical solution given by Eqs. A.1 and A.2, respectively. As shown in Fig. A.1, the purple dots are collected from the numerical simulations whereas the solid lines represent the corresponding analytical so lutions. It can be seen from the two figures that the analytical so lution approximates zero when the separation distance becomes larger, and the force maintains a constant value when the separa tion distance is smaller than the cutoff distance $h_{\min}$. For both van der Waals interactions between two particles and a particle with a wall, the newly implemented model shows perfect agreement with the results given by the analytical solutions in Eqs. A.1 and A.2.

Table A.1
Parameters for validations of the van der Waals force model.

Parameter [Unit]	Value
R_i [m]	5×10^{-6}
R_j [m]	5×10^{-6}
ρ [kg/m^3]	2500
$h_{\min}$ [m]	1.0×10^{-8}
γ_s [J/m^2]	0.86×10^{-3}
Y [kg/(m $\cdot$s^2)]	1.0×10^{7}
ν [ ]	0.29

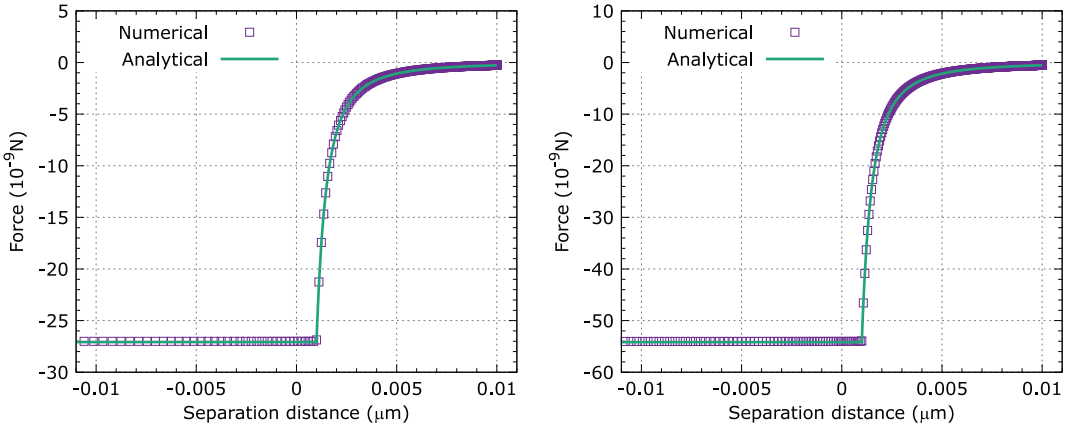

Fig. A.1. Validations of the van der Waals force model: (a) particle to particle, (b) particle to wall.

Voronoi tessellation for granular media: calculations of the local packing fraction with Voro++

Voronoi tessellation is used to calculate the local packing properties, e.g. the local packing fraction and packing structures of either mono disperse or poly disperse granular systems in this work. The local packing fraction φ_f is defined by

$$\varphi_f \quad \frac{V_s}{V_c}, \tag{A.4}$$

where V_s and V_c are the volume of the sphere and its voronoi cell, respectively. The open source Voronoi tessellation code Voro++ is used to generate voronoi cells and calculate the volume of each voronoi cell.

Two different cases are presented to demonstrate the per formance of the Voro++ code in calculating the local packing fractions for the Simple Cubic Packing (SCP) and Hexagonal Close Packing (HCP). A single layer of SCP is shown in Fig. A.2. for which the analytical solution of the packing fraction is given by

$$\varphi_f^{\mathrm{SCP}} \quad \frac{V_p}{V_c} \quad \frac{\frac{4\pi R^3}{3}}{(2R)^3} \quad \frac{\pi}{6} \quad 0.5236. \tag{A.5}$$

The image on the right hand side of Fig. A.2 is the colour map of the local packing fraction of the SCP. It proves that the local packing fraction calculated with Voro++ agrees well with the corre sponding analytical solution.

Similarly, a single layer of HCP is shown in Fig. A.3, where a periodic boundary condition is applied along the horizontal direc tion. The analytical solution for the single layer HCP except for the local packing fraction on the boundary is given by

$$\varphi_f^{\mathrm{HCP}} \quad \frac{V_p}{V_c} \quad \frac{\frac{4\pi R^3}{3}}{\frac{3\sqrt{3}\left(\frac{2R}{\sqrt{3}}\right)^2 2R}{2}} \quad \frac{\pi}{3\sqrt{3}} \quad 0.6046. \tag{A.6}$$

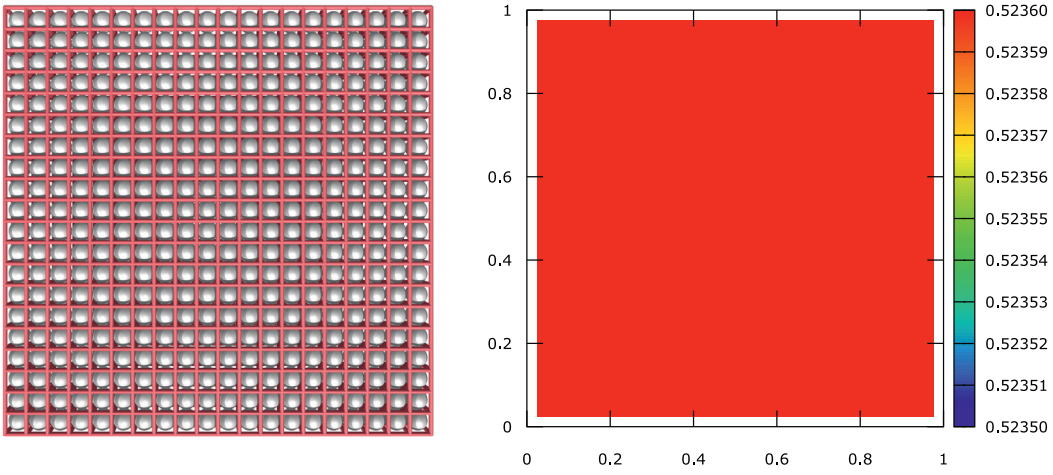

Fig. A.2. (a) voronoi cells of the SCP, (b) local packing fraction of SCP.

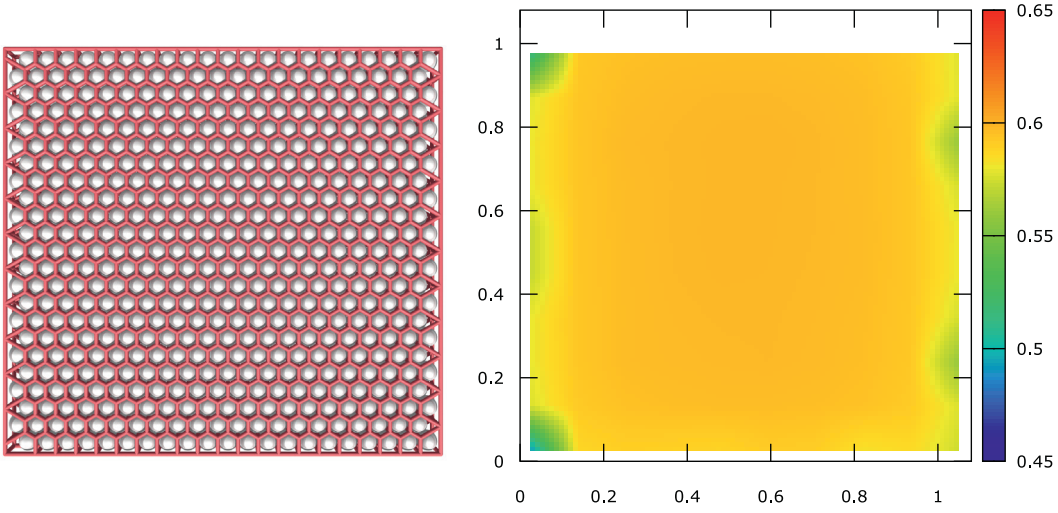

Fig. A.3. (a) voronoi cells of the HCP, (b) local packing fraction of HCP.

The local packing fraction calculated by Voro++ is shown in the right hand side of Fig. A.3, where a good agreement is found between the local packing fraction calculated by Voro++ and the analytical solution.

References

Abbasfard, H., Evans, G., & Moreno-Atanasio, R. (2016). Effect of van der Waals force cut-off distance on adhesive collision parameters in DEM simulation. *Powder Technology, 299*, 9–18.

Balachandran Nair, A. N., Pirker, S., & Saeedipour, M. (2021). Resolved CFD-DEM simulation of blood flow with a reduced-order RBC model. *Computational Particle Mechanics*, 1–16.

Brackbill, J. U., Kothe, D. B., & Zemach, C. (1992). A continuum method for modeling surface tension. *Journal of Computational Physics, 100*(2), 335–354.

Breugem, W.-P. (2012). A second-order accurate immersed boundary method for fully resolved simulations of particle-laden flows. *Journal of Computational Physics, 231*(13), 4469–4498.

Brown, P. P., & Lawler, D. F. (2003). Sphere drag and settling velocity revisited. *Journal of Environmental Engineering, 129*(3), 222–231.

Christodoulou, C., Sorensen, E., Khair, A., García-Munoz, S., & Mazzei, L. (2020). A model for the fluid dynamic behavior of a film coating suspension during tablet coating. *Chemical Engineering Research and Design, 160*, 301–320.

Davydzenka, T., Fagbemi, S., & Tahmasebi, P. (2020). Coupled fine-scale modeling of the wettability effects: Deformation and fracturing. *Physics of Fluids, 32*(8), 083308.

D. Computing, CFDEM®coupling. (2017). *Open source CFD-DEM coupling*. URL https://github.com/CFDEMproject/CFDEMcoupling-PUBLIC.git.

D. Computing, LIGGGHTS. (2015). *DEM simulation engine*. URL https://github.com/CFDEMproject/LIGGGHTS-PUBLIC.

Deegan, R. D., Bakajin, O., Dupont, T. F., Huber, G., Nagel, S. R., & Witten, T. A. (1997). Capillary flow as the cause of ring stains from dried liquid drops. *Nature, 389*(6653), 827–829.

Derby, B. (2015). Additive manufacture of ceramics components by inkjet printing. *Engineering, 1*(1), 113–123.

Fang, J., Wang, L., Hong, Y., & Zhao, J. (2022). Influence of solid–fluid interaction on impact dynamics against rigid barrier: CFD-DEM modelling. *Géotechnique, 72*(5), 391–406.

Fujita, M., Koike, O., & Yamaguchi, Y. (2013). Computation of capillary interactions among many particles at free surface. *Applied Physics Express, 6*(3), 036501.

Fujita, M., Koike, O., & Yamaguchi, Y. (2015). Direct simulation of drying colloidal suspension on substrate using immersed free surface model. *Journal of Computational Physics, 281*, 421–448.

Gabriel, E., Fagg, G. E., Bosilca, G., Angskun, T., Dongarra, J. J., Squyres, J. M., Sahay, V., Kambadur, P., Barrett, B., Lumsdaine, A., Castain, R. H., Daniel, D. J., Graham, R. L., & Woodall, T. S. (2004). Open MPI: Goals, concept, and design of a next generation mpi implementation. In *Recent advances in parallel virtual machine and message passing interface: 11th European PVM/MPI users' group meeting Budapest, Hungary, September 19-22, 2004. Proceedings 11* (pp. 97–104). Springer.

Galusinski, C., & Vigneaux, P. (2008). On stability condition for bifluid flows with surface tension: Application to microfluidics. *Journal of Computational Physics, 227*(12), 6140–6164.

Giuliano, L. V., Buffo, A., Vanni, M., & Frungieri, G. (2023). Micromechanics and strength of agglomerates produced by spray drying. *JCIS Open, 9*, 100068.

Golshan, S., Sotudeh-Gharebagh, R., Zarghami, R., Mostoufi, N., Blais, B., & Kuipers, J. (2020). Review and implementation of CFD-DEM applied to chemical process systems. *Chemical Engineering Science, 221*, 115646.

Gong, Z., Wu, Z., An, C., Zhang, B., & Fu, X. (2023). CP3d: A comprehensive euler-Lagrange solver for direct numerical simulation of particle-laden flows. *Computer Physics Communications, 286*, 108666.

Gotzinger, M., & Peukert, W. (2003). Dispersive forces of particle-surface interactions: Direct AFM measurements and modelling. *Powder Technology, 130*(1–3), 102–109.

Hager, A. (2014). *CFD-DEM on multiple scales: An extensive investigation of particle-fluid interactions*. Ph.D. thesis, Johannes Kepler University Linz.

Hager, A., Kloss, C., Pirker, S., & Goniva, C. (2014). Parallel resolved open source CFD-DEM: Method, validation and application. *The Journal of Computational Multiphase Flows, 6*(1), 13–27.

Hamaker, H. C. (1937). The London–van der Waals attraction between spherical particles. *Physica, 4*(10), 1058–1072.

Irfan, M., & Muradoglu, M. (2017). A front tracking method for direct numerical simulation of evaporation process in a multiphase system. *Journal of Computational Physics, 337*, 132–153.

Kieckhefen, P., Lichtenegger, T., Pietsch, S., Pirker, S., & Heinrich, S. (2019). Simulation of spray coating in a spouted bed using recurrence CFD. *Particuology, 42*, 92–103.

Koos, E. (2014). Capillary suspensions: Particle networks formed through the capillary force. *Current Opinion in Colloid & Interface Science, 19*(6), 575–584.

Kuang, S., Zhou, M., & Yu, A. (2020). CFD-DEM modelling and simulation of pneumatic conveying: A review. *Powder Technology, 365*, 186–207.

Lafaurie, B., Nardone, C., Scardovelli, R., Zaleski, S., & Zanetti, G. (1994). Modelling merging and fragmentation in multiphase flows with SURFER. *Journal of Computational Physics, 113*(1), 134–147.

Lai, Z., Zhao, J., Zhao, S., & Huang, L. (2023). Signed distance field enhanced fully resolved CFD-DEM for simulation of granular flows involving multiphase fluids and irregularly shaped particles. *Computer Methods in Applied Mechanics and Engineering, 414*, 116195.

Ledesma-Aguilar, R., Vella, D., & Yeomans, J. M. (2014). Lattice-Boltzmann simulations of droplet evaporation. *Soft Matter, 10*(41), 8267–8275.

Li, Y., Xu, Y., & Thornton, C. (2005). A comparison of discrete element simulations and experiments for 'sandpiles' composed of spherical particles. *Powder Technology, 160*(3), 219–228.

Lohse, D. (2022). Fundamental fluid dynamics challenges in inkjet printing. *Annual Review of Fluid Mechanics, 54*, 349–382.

Lu, L., Gao, X., Dietiker, J.-F., Shahnam, M., & Rogers, W. A. (2022). MFiX based multi-scale CFD simulations of biomass fast pyrolysis: A review. *Chemical Engineering Science, 248*, 117131.

Ma, H., Zhou, L., Liu, Z., Chen, M., Xia, X., & Zhao, Y. (2022). *A review of recent development for the CFD-DEM investigations of non-spherical particles*. Powder Technology, 117972.

Mikolajek, M., Reinheimer, T., Muth, M., Hohwieler, P., Hoffmann, M. J., & Binder, J. R. (2018). Control of the surface morphology of ceramic/polymer composite inks for inkjet printing. *Advanced Engineering Materials, 20*(9), 1800318.

Mino, Y., Tanaka, C., Tanaka, H., Nakaso, K., & Gotoh, K. (2022). Numerical simulation of a drying colloidal suspension on a wettable substrate using the lattice Boltzmann method. *Chemical Engineering Science, 263*, 118050.

Nguyen, G. T., Chan, E. L., Tsuji, T., Tanaka, T., & Washino, K. (2021). Interface control for resolved CFD-DEM with capillary interactions. *Advanced Powder Technology, 32*(5), 1410–1425.

Norouzi, H. R., Zarghami, R., Sotudeh-Gharebagh, R., & Mostoufi, N. (2016). *Coupled CFD-DEM modeling: Formulation, implementation and application to multiphase flows*. John Wiley & Sons.

O. Foundation. (2018). *OpenFOAM-5.x*. URL https://github.com/OpenFOAM/OpenFOAM-5.x.

Palmore, J., Jr., & Desjardins, O. (2019). A volume of fluid framework for interface-resolved simulations of vaporizing liquid-gas flows. *Journal of Computational Physics, 399*, 108954.

Patankar, N. A., Singh, P., Joseph, D. D., Glowinski, R., & Pan, T.-W. (2000). A new formulation of the distributed Lagrange multiplier/fictitious domain method for particulate flows. *International Journal of Multiphase Flow, 26*(9), 1509–1524.

Podlozhnyuk, A. (2018). *Modelling superquadric particles in DEM and CFD-DEM: Implementation, validation and application in an open-source framework, Ph.D. Thesis*. Johannes Kepler University Linz.

Podlozhnyuk, A., Pirker, S., & Kloss, C. (2017). Efficient implementation of superquadric particles in discrete element method within an open-source framework. *Computational Particle Mechanics, 4*(1), 101–118.

Rusche, H. (2003). *Computational fluid dynamics of dispersed two-phase flows at high phase fractions, Ph.D. thesis*. Imperial College London.

Schnorr Filho, E. A., Lima, N. C., & Franklin, E. M. (2022). Resolved CFD-DEM simulations of the hydraulic conveying of coarse grains through a very-narrow elbow. *Powder Technology, 395*, 811–821.

Shen, Z., Wang, G., Huang, D., & Jin, F. (2022). A resolved CFD-DEM coupling model for modeling two-phase fluids interaction with irregularly shaped particles. *Journal of Computational Physics, 448*, 110695.

Shirgaonkar, A. A., MacIver, M. A., & Patankar, N. A. (2009). A new mathematical formulation and fast algorithm for fully resolved simulation of self-propulsion. *Journal of Computational Physics, 228*(7), 2366–2390.

Ten Cate, A., Nieuwstad, C., Derksen, J., & Van den Akker, H. (2002). Particle imaging velocimetry experiments and Lattice-Boltzmann simulations on a single sphere settling under gravity. *Physics of Fluids, 14*(11), 4012–4025.

Tryggvason, G., Scardovelli, R., & Zaleski, S. (2011). *Direct numerical simulations of gas–liquid multiphase flows*. Cambridge University Press.

Uhlmann, M. (2005). An immersed boundary method with direct forcing for the simulation of particulate flows. *Journal of Computational Physics, 209*(2), 448–476.

Uzi, A., Ostrovski, Y., & Levy, A. (2016). Modeling and simulation of particles in gas-liquid interface. *Advanced Powder Technology, 27*(1), 112–123.

Washino, K., Chan, E. L., Tsujimoto, T., Tsuji, T., & Tanaka, T. (2023). Development of resolved CFD-DEM coupling model for three-phase flows with non-spherical particles. *Chemical Engineering Science, 267*, 118335.

Washino, K., Tan, H., Hounslow, M., & Salman, A. (2013). A new capillary force model implemented in micro-scale CFD-DEM coupling for wet granulation. *Chemical Engineering Science, 93*, 197–205.

Wu, M., Peters, B., Rosemann, T., & Kruggel-Emden, H. (2020). A forcing fictitious domain method to simulate fluid-particle interaction of particles with superquadric shape. *Powder Technology, 360*, 264–277.

Xia, H. (2023). *An improved CFD-DEM framework for gas-liquid-solid multiphase free surface flow, Ph.D. thesis*. Karlsruhe Institute of Technology (KIT).

Xia, H., & Kamlah, M. (2024). An improved Coupled Level Set and Volume of Fluid (i-CLSVoF) framework for sessile droplet evaporation. *Journal of Computational Science, 75*, 102195.

Yang, D.-L., Liu, R.-K., Wei, Y., Sun, Q., & Wang, J.-X. (2023). Micro-sized nano-aggregates: Spray-drying-assisted fabrication and applications. *Particuology, 85*, 22 48.

Yang, R., Zou, R., & Yu, A. (2000). Computer simulation of the packing of fine particles. *Physical Review, 62*(3), 3900.

Yu, T., & Zhao, J. (2021). Semi-coupled resolved CFD-DEM simulation of powder-based selective laser melting for additive manufacturing. *Computer Methods in Applied Mechanics and Engineering, 377*, 113707.

Zhang, Y., Xu, J., Chang, Q., Zhao, P., Wang, J., & Ge, W. (2023). Numerical simulation of fluidization: Driven by challenges. *Powder Technology, 414*, 118092.

Zhang, C., Zhang, H., Zhao, Y., & Yang, C. (2021). An immersed boundary-lattice Boltzmann model for simulation of deposited particle patterns in an evaporating sessile droplet with dispersed particles. *International Journal of Heat and Mass Transfer, 181*, 121905.

Zhao, T. (2014). *Investigation of landslide-induced debris flows by the DEM and CFD, Ph.D. thesis*. University of Oxford.